Physical Properties of Kuiper Belt and Centaur Objects: Constraints from the Spitzer Space Telescope

John Stansberry
University of Arizona

Will Grundy
Lowell Observatory

Mike Brown
California Institute of Technology

Dale Cruikshank
NASA Ames Research Center

John Spencer
Southwest Research Institute

David Trilling
University of Arizona

Jean-Luc Margot
Cornell University

Detecting heat from minor planets in the outer solar system is challenging, yet it is the most efficient means for constraining the albedos and sizes of Kuiper belt objects (KBOs) and their progeny, the Centaur objects. These physical parameters are critical, e.g., for interpreting spectroscopic data, deriving densities from the masses of binary systems, and predicting occultation tracks. Here we summarize Spitzer Space Telescope observations of 47 KBOs and Centaurs at wavelengths near 24 and 70 μm. We interpret the measurements using a variation of the standard thermal model (STM) to derive the physical properties (albedo and diameter) of the targets. We also summarize the results of other efforts to measure the albedos and sizes of KBOs and Centaurs. The three or four largest KBOs appear to constitute a distinct class in terms of their albedos. From our Spitzer results, we find that the geometric albedo of KBOs and Centaurs is correlated with perihelion distance (darker objects having smaller perihelia), and that the albedos of KBOs (but not Centaurs) are correlated with size (larger KBOs having higher albedos). We also find hints that albedo may be correlated with visible color (for Centaurs). Interestingly, if the color correlation is real, redder Centaurs appear to have higher albedos. Finally, we briefly discuss the prospects for future thermal observations of these primitive outer solar system objects.

1. INTRODUCTION

The physical properties of Kuiper belt objects (KBOs) remain poorly known nearly 15 years after the discovery of (15760) 1992 QB_1 (*Jewitt and Luu,* 1993). While KBOs can be discovered, their orbits determined, and their visible-light colors measured (to some extent) using modest telescopes, learning about fundamental properties such as size, mass, albedo, and density remains challenging. Determining these properties for a representative sample of transneptunian objects (TNOs) is important for several reasons. Estimating the total mass of material in the transneptunian region and relating visible magnitude frequency distributions to size- and mass-frequency is uncertain, at best. Quantitative interpretation of visible and infrared spectra is impossible without knowledge of the albedo in those wavelength ranges. Size estimates, when coupled with masses determined for binary KBOs (see the chapter by Noll et al.), constrain the density, and hence internal composition and structure, of these objects. All these objectives have important implications for physical and chemical conditions in the outer protoplanetary nebula, for the accretion of solid objects in the outer solar

system, and for the collisional evolution of KBOs themselves. Of course, there is a relative wealth of information about Pluto and Charon, the two longest known KBOs, and we do not address their properties further here.

The Centaur objects, with orbits that cross those of one or more of the giant planets, are thought to be the dynamical progeny of KBOs (e.g., *Levison and Duncan,* 1997). The Centaurs are particularly interesting both because of their direct relation to KBOs, and also because their orbits bring them closer to the Sun and to observers, where, for a given size, they are brighter at any wavelength than their more distant relatives. Because of their planet-crossing orbits, the dynamical lifetimes of Centaurs are relatively short, typically a few million years (e.g., *Horner et al.,* 2004).

The sizes of some KBOs and Centaurs have been determined by a variety of methods. Using the Hubble Space Telescope (HST), *Brown and Trujillo* (2004) resolved the KBO 50000 Quaoar, placed an upper limit on the size of Sedna (*Brown et al.,* 2004), and resolved Eris (*Brown et al.,* 2006). Recently *Rabinowitz et al.* (2005) placed constraints on the size and albedo of 136199 (2003 EL_{61}) based on its short rotation period (3.9 h) and an analysis of the stability of a rapidly rotating ellipsoid. *Trilling and Bernstein* (2006) performed a similar analysis of the lightcurves of a number of small KBOs, obtaining constraints on their sizes and albedos. Advances in the sensitivity of far-IR and submillimeter observatories have recently allowed the detection of thermal emission from a sample of outer solar system objects, providing constraints on their sizes and albedos. *Jewitt et al.* (2001), *Lellouch et al.* (2002), *Margot et al.* (2002, 2004), *Altenhoff et al.* (2004), and *Bertoldi et al.* (2006) have reported submillimeter to millimeter observations of thermal emission from KBOs. *Sykes et al.* (1991, 1999) analyze Infrared Astronomical Satellite (IRAS) thermal detections of 2060 Chiron and the Pluto-Charon system, determining their sizes and albedos. Far-infrared data from the Infrared Space Observatory (ISO) were used to determine the albedos and diameters of KBOs 15789 (1993 SC), 15874 (1996 TL_{66}) (*Thomas et al.,* 2000), and 2060 Chiron (*Groussin et al.,* 2004). *Lellouch et al.* (2000) studied the thermal state of Pluto's surface in detail using ISO. *Grundy et al.* (2005) provide a thorough review of most of the above, and include a sample of binary KBO systems with known masses, to constrain the sizes and albedos of 20 KBOs.

Spitzer Space Telescope (Spitzer hereafter) thermal observations of KBOs and Centaurs have previously been reported by *Stansberry et al.* (2004) (29P/Schwassmann-Wachmann 1), *Cruikshank et al.* (2005) (55565 2002 AW_{197}), *Stansberry et al.* (2006) (47171 1999 TC_{36}), *Cruikshank et al.* (2006), *Grundy et al.* (2007) (65489 2003 FX_{128}), and Grundy et al. (in preparation) (42355 Typhon). Here we summarize results from several Spitzer programs to measure the thermal emission from 47 KBOs and Centaurs. These observations place secure constraints on the sizes and albedos of 42 objects, some overlapping with determinations based on other approaches mentioned above. We present initial conclusions regarding the relationship between albedo and orbital and physical properties of the targets, and discuss future prospects for progress in this area.

2. THERMAL MODELING

Measurements of thermal emission can be used to constrain the sizes, and thereby albedos, of unresolved targets. *Tedesco et al.* (1992; 2002) used IRAS thermal detections of asteroids to build a catalog of albedos and diameters. Visible observations of the brightness of an unresolved object are inadequate to determine its size, because that brightness is proportional to the product of the visible geometric albedo, p_V, and the cross-sectional area of the target. Similarly, the brightness in the thermal IR is proportional to the area, and is also a function of the temperature of the surface, which in turn depends on the albedo. Thus, measurements of both the visible and thermal brightness can be combined to solve for both the size of the target and its albedo. Formally the method requires the simultaneous solution of the following two equations

$$F_{vis} = \frac{F_{\odot,vis}}{(r/1\ AU)^2} R^2 p_V \frac{\Phi_{vis}}{\Delta^2} \quad (1a)$$

$$F_{ir} = \frac{R^2 \Phi_{ir}}{\pi \Delta^2} \varepsilon \int B_\lambda(T(\theta,\phi)) \sin\theta d\theta d\phi \quad (1b)$$

where F is the measured flux density of the object at a wavelength in the visible ("vis") or thermal-infrared ("ir"); $F_{\odot,vis}$ is the visible-wavelength flux density of the Sun at 1 AU; r and Δ are the object's heliocentric and geocentric distances, respectively; R is the radius of the body (assumed to be spherical); p_V is the geometric albedo in the visible; Φ is the phase function in each regime; B_λ is the Planck function; and ε is the infrared bolometric emissivity. $T = T(p_V q, \eta, \varepsilon, \theta, \phi)$ is the temperature, which is a function of p_V; ε; the "beaming parameter," η; surface planetographic coordinates θ and ϕ; and the (dimensionless) phase integral, q (see below for discussions of η and q).

In practice, the thermal flux depends sensitively on the temperature distribution across the surface of the target, and uncertainties about that temperature distribution typically dominate the uncertainties in the derived albedos and sizes (see Fig. 1). Given knowledge of the rotation vector, shape, and the distribution of albedo and thermal inertia, it is in principle possible to compute the temperature distribution. Not surprisingly, none of these things are known for a typical object where we seek to use the radiometric method to measure the size and albedo. The usual approach is to use a simplified model to compute the temperature distribution based on little or no information about the object's rotation axis or even rotation period.

2.1. Standard Thermal Model

The most commonly employed model for surface temperature on asteroidal objects is the standard thermal model (STM) (cf. *Lebofsky and Spencer,* 1989, and references therein). The STM assumes a nonrotating (or equivalently, zero thermal inertia) spherical object, and represents the "hot" end member to the suite of possible temperature dis-

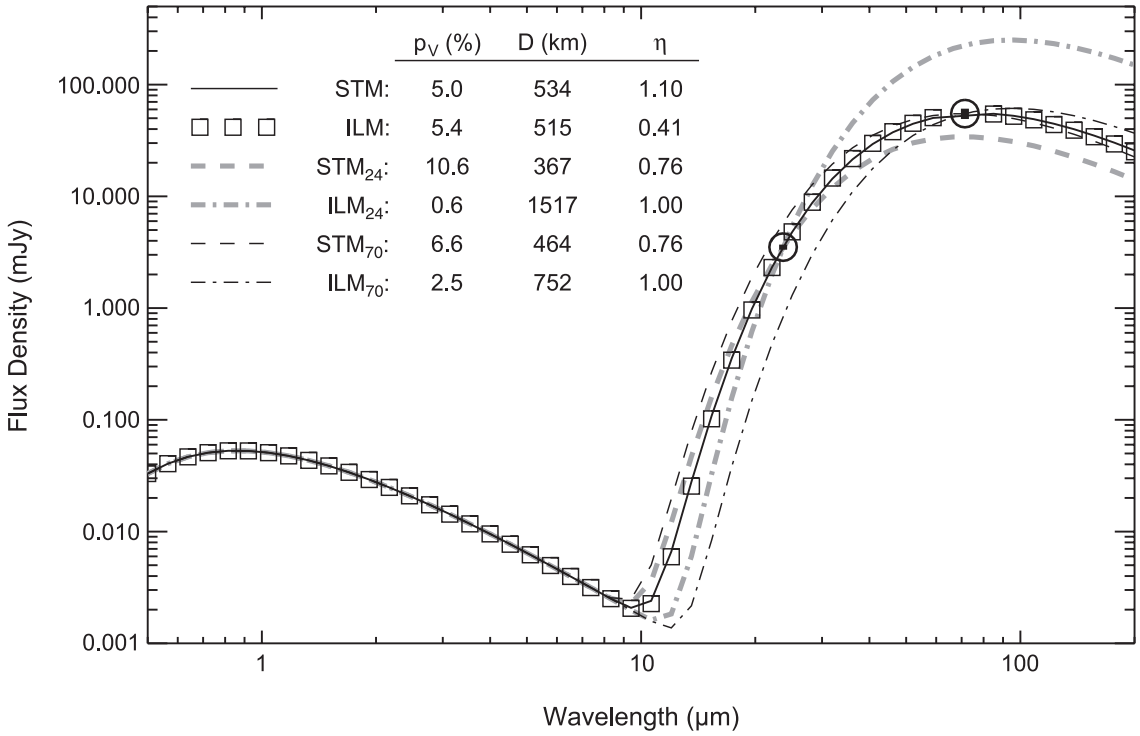

Fig. 1. Thermal models for KBO 38628 Huya (2000 EB_{173}). Spitzer Space Telescope 24- and 70-μm data are shown as circles, with vertical error bars within them indicating the measurement uncertainties. Six models are fit to the data, with the resulting model albedos, diameters, and beaming parameters summarized in the legend. From top to bottom the models are: (1) hybrid STM fit to 24- and 70-μm data, with η as a free parameter (the therm model used here); (2) hybrid ILM fit to 24- and 70-μm data; (3) canonical STM (η = 0.756) fit to the 24-μm data; (4) canonical ILM (η = 1.0) fit to the 24-μm data; (5) canonical STM fit to the 70-μm data; (6) canonical ILM fit to the 70-μm data. Note the close agreement of the albedos and sizes for models 1 and 2. Fits to data from one band, using the canonical asteroid values for η, result in much larger uncertainties in the derived parameters, particularly the fits to the 24-μm data.

tributions. Under STM assumptions, the dayside temperature depends only on the angular distance from the subsolar point, θ: $T(\theta) = T_0\cos^{1/4}\theta$, and the temperature is zero on the nightside. The subsolar point temperature $T_0 = [(1 - A)S/(\eta\varepsilon\sigma)]^{1/4}$. Here $A = qp_V$ is the bolometric albedo, S is the solar constant at the distance of the object, and σ is the Stefan-Boltzmann constant. Even though the STM represents the hottest reasonable distribution of surface temperatures for an object in radiative equilibrium with sunlight, early studies of the emission from asteroids showed that their emission was even hotter than predicted by the STM (*Jones and Morrison,* 1974; *Morrison and Lebofsky,* 1979). That led to the introduction of the beaming parameter, η, which allows for localized temperature enhancements on the dayside, e.g., in the bottoms of craters or other rough features, and the tendency of such warm regions to radiate preferentially in the sunward (and, for outer solar system objects, observerward) direction (i.e., to beam). (Note that while η appears analogously to the emissivity, ε, in the expression for the surface temperature, η does not appear explicitly in the expression for the thermal emission; equation (1b).) *Lebofsky et al.* (1986) derived a value of η = 0.756 based on 10-μm observations of Ceres and Pallas. We refer to the STM with η set to 0.756 as the *canonical STM*.

2.2. Isothermal Latitude Model

The cold end member of the suite of plausible temperature distributions for an object in radiative equilibrium with sunlight is the isothermal latitude model (ILM; also known as the fast-rotator model). The ILM assumes a spherical object illuminated at the equator and rotating very quickly (or equivalently, a slowly rotating object with infinite thermal inertia). The resulting temperature distribution depends only on latitude, φ: $T(\phi) = T_0\cos^{1/4}\phi$, where in this case the subsolar point temperature is given by $T_0 = [(1 - A)S/(\pi\eta\varepsilon\sigma)]^{1/4}$. The factor of π in this expression reduces the subsolar point temperature by 33% relative to the STM. Because the ILM is characterized by infinite thermal inertia, local temperature variations, and therefore beaming, are precluded; thus the *canonical ILM* assumes η = 1.

2.3. Hybrid Thermal Model

Figure 1 illustrates the problems inherent in using either the STM or the ILM to measure the sizes and albedos of KBOs. In particular, none of the four canonical STM or ILM models fit to either the 24- or 70-μm data (four lower elements in the figure legend) match the observed 24:70-μm

color. As a result, the systematic uncertainties on the albedos and diameters, depending only on whether the STM or ILM is used, are large: p_V is uncertain by a factor >2.5 for the fits to the 70-μm data, and is uncertain by a factor of >17 for the fits to the 24-μm data. (Note, however, that the relative efficacy of these two wavelengths depends on the temperature of the target: If the thermal spectrum peaks near the 24-μm band, observations at that wavelength will be considerably more effective at constraining the physical properties of the target than indicated by this particular example.) However, if the beaming parameter, η, is allowed to be a free parameter of the fit (top two elements in the figure legend), both the color of the thermal emission and its intensity can be matched. More importantly, both the STM and ILM give nearly the same diameters and albedos with η as a free parameter. The basic reason for this is that the 24- and 70-μm data provide a direct determination of the temperature of the thermal emission from the object; equating that color temperature to the effective temperature gives a direct estimate of the size of the target, independent of the details of an assumed temperature distribution (and independent of the visual brightness as well).

While the beaming parameter was introduced to model enhanced localized dayside temperatures and infrared beaming, it can also mimic the effects of other influences on the temperature distribution, such as pole orientation (note that the emission from a pole-on ILM is indistinguishable from the STM), and intermediate rotation rates and thermal inertias. For example, a rotating body with nonzero thermal inertia will have lower dayside temperatures than predicted by the STM, but an STM with a value of η larger than would be supposed based on its surface roughness will have a similar color temperature. Likewise, a quickly rotating body with a low thermal inertia will have higher dayside temperatures than predicted by the ILM, an effect that can be mimicked by an ILM with $\eta < 1$.

Returning to the top two models in the legend of Fig. 1, the STM fit results in $\eta = 1.09$, suggesting that the temperature distribution on the target (the KBO 36828 Huya) is cooler than predicted by the canonical STM with $\eta = 0.756$. Likewise, for the ILM $\eta = 0.41$, suggesting that the surface is significantly hotter than would be predicted by the canonical ILM with $\eta = 1$.

2.4. Thermal Model: Application

In the following we adopt a thermal model in which the beaming parameter, along with size and albedo, are free parameters that we use to simultaneously fit observed flux densities at two thermal wavelengths, and the constraint imposed by the visual brightness of the object. Because such models have temperature distributions intermediate between the canonical STM and ILM, they can be thought of as a hybrid between the two. Furthermore, because the systematic uncertainties in the model albedos and diameters associated with the choice of hybrid STM or hybrid ILM are fairly small relative to the uncertainties in the measured flux densities and other model assumptions, we simply adopt the hybrid STM as our model of choice. (The error bars on p_V and D stemming from the choice of STM or ILM hybrid model in Fig. 1 are ≤4% and ≤2%.) We note that a number of studies have employed a similar approach with variable η (e.g., *Harris,* 1998; *Delbo et al.,* 2003; *Fernández et al.,* 2003).

In order to use the STM, we must make some assumptions regarding the nature of the thermal emission and visible scattering. We assume a gray emissivity, $\varepsilon = 0.9$. The infrared phase function, $\Phi_{ir} = 0.01$ mag/deg, depends only weakly on the emission angle. For our observations, emission angles for all but five targets (29P, Asbolus, Elatus, Thereus, and Okyrhoe) were <5°. Because the effects are small relative to other uncertainties in the models and data, we have neglected the IR phase effect for all the results presented here. We assume standard scattering behavior for the the objects in the visible, i.e., a scattering assymetry parameter, G = 0.15, leading to a phase integral q = 0.39 (*Bowell et al.,* 1989). This assumption also allows us to directly relate the geometric albedo p_V, the diameter D, and the absolute visual magnitude, H_V via $D = 1346\, p_V^{1/2} 10^{-H_V/5}$, where D is in km (*Bowell et al.,* 1989; *Harris,* 1998). By utilizing the absolute visual magnitude in this way, the scattering phase function, Φ_{vis}, apparently drops out; however, if the actual scattering behavior differs from the assumption above, our albedos and diameters will still be affected because the scattering behavior determines the value of q. We note, also, the results of *Romanishin and Tegler* (2005), who found that absolute magnitudes available through the IAU Minor Planet Center and through the Horizons service at the Jet Propulsion Laboratory have are biased downward (brighter) by 0.3 mag. The H_V values shown in Table 1 are culled from the photometric literature, and should be fairly reliable.

For low-albedo objects, the albedos we derive depend only weakly on the assumed value of q, while for high-albedo objects the value of q exerts a strong influence (see expressions for T_0 in sections 2.1 and 2.2). For the example of 38628 Huya (Fig. 1), changing to q = 0.8 makes only a ≤1% difference in the albedo. However, if we use q = 0.39 to model the data for the four largest objects in the sample — 90377 Sedna, 136199 Eris, 136108 (2003 EL_{61}), and 136472 (2005 FY_9) — we obtain geometric albedos that exceed a value of 2. While not (necessarily) unphysical, such high values for the geometric albedo are unprecedented. Pluto's phase integral q = 0.8, so for these four objects (only) we adopt that value instead.

2.5. Thermophysical Models

More sophisticated extensions to the STM and ILM include the effects of surface roughness and (nonzero, noninfinite) thermal inertia (*Spencer,* 1990), and viewing geometries that depart significantly from zero phase (*Harris,* 1998). However, for the purpose of determining KBO albedos and diameters from their thermal emission, the hybrid

TABLE 1. Orbital and photometric properties.

Number*	Designation*	Name*	a (AU)†	e†	i†	H_V‡	S‡	σ_S‡	TNO?§	Class¶
29P	Schwassmann-Wachmann 1		5.986	0.04	9.39	11.10	15.75	1.10	N	CENTR
2060	1977 UB	Chiron	13.690	0.38	6.93	6.58	1.85	1.18	N	CENTR
5145	1992 AD	Pholus	20.426	0.57	24.68	7.63	50.72	2.44	N	CENTR
7066	1993 HA_2	Nessus	24.634	0.52	15.65	9.7	34.03	9.25	N	CENTR
8405	1995 GO	Asbolus	17.986	0.62	17.64	9.15	19.88	8.58	N	CENTR
10199	1997 CU_{26}	Chariklo	15.865	0.18	23.38	6.66	12.95	1.38	N	CENTR
10370	1995 DW_2	Hylonome	25.202	0.25	4.14	9.41	9.29	2.28	N	CENTR
15820	1994 TB		39.288	0.31	12.14	8.00	40.92	2.87	Y	RESNT
15874	1996 TL_{66}		82.756	0.58	24.02	5.46	0.13	2.24	Y	SCTNR
15875	1996 TP_{66}		39.197	0.33	5.69	7.42	26.52	6.80	Y	RESNT
20000	2000 WR_{106}	Varuna	42.921	0.05	17.20	3.99	23.91	1.25	Y	CLSCL
26308	1998 SM_{165}		47.468	0.37	13.52	6.38	27.77	1.91	Y	RESNT
26375	1999 DE_9		55.783	0.42	7.62	5.21	20.24	3.46	Y	RESNT
28978	2001 KX_{76}	Ixion	39.648	0.24	19.59	3.84	22.90	1.60	Y	RESNT
29981	1999 TD_{10}		95.040	0.87	5.96	8.93	10.37	1.88	Y	CENTR
31824	1999 UG_5	Elatus	11.778	0.38	5.25	10.52	27.75	0.97	N	CENTR
32532	2001 PT_{13}	Thereus	10.617	0.20	20.38	9.32	10.79	0.96	N	CENTR
35671	1998 SN_{165}		37.781	0.04	4.62	5.72	5.05	1.95	Y	CLSCL
38628	2000 EB_{173}	Huya	39.773	0.28	15.46	5.23	22.20	4.80	Y	RESNT
42355	2002 CR_{46}	Typhon	38.112	0.54	2.43	7.65	15.87	1.93	Y	CENTR
47171	1999 TC_{36}		39.256	0.22	8.42	5.39	35.24	2.82	Y	RESNT
47932	2000 GN_{171}		39.720	0.29	10.80	6.2	24.78	3.41	Y	RESNT
50000	2002 LM_{60}	Quaoar	43.572	0.04	7.98	2.74	28.15	1.81	Y	CLSCL
52872	1998 SG_{35}	Okyrhoe	8.386	0.31	15.64	11.04	11.72	5.08	N	CENTR
52975	1998 TF_{35}	Cyllarus	26.089	0.38	12.66	9.01	36.20	2.42	N	CENTR
54598	2000 QC_{243}	Bienor	16.472	0.20	20.76	7.70	6.86	3.17	N	CENTR
55565	2002 AW_{197}		47.349	0.13	24.39	3.61	22.00	2.21	Y	SCTNR
55576	2002 GB_{10}	Amycus	25.267	0.40	13.34	8.07	32.13	4.35	N	CENTR
55636	2002 TX_{300}		43.105	0.12	25.87	3.49	-0.96	1.20	Y	SCTNR
55637	2002 UX_{25}		42.524	0.14	19.48	3.8	26.61	10.90	Y	SCTNR
60558	2000 EC_{98}	174P/Echeclus	10.771	0.46	4.33	9.55	10.43	4.83	N	CENTR
63252	2001 BL_{41}		9.767	0.29	12.45	11.47	14.37	2.75	N	CENTR
65489	2003 FX_{128}	Ceto	102.876	0.83	22.27	6.60	20.72	2.84	Y	CENTR
73480	2002 PN_{34}		30.966	0.57	16.64	8.66	16.21	1.90	Y	CENTR
83982	2002 GO_9	Crantor	19.537	0.28	12.77	9.16	42.19	4.43	N	CENTR
84522	2002 TC_{302}		55.027	0.29	35.12	4.1			Y	SCTNR
84922	2003 VS_2		39.273	0.07	14.79	4.4			Y	RESNT
90377	2003 VB_{12}	Sedna	489.619	0.84	11.93	1.8	33.84	3.62	Y	SCEXT
90482	2004 DW	Orcus	39.363	0.22	20.59	2.5	1.06	1.05	Y	RESNT
90568	2004 GV_9		42.241	0.08	21.95	4.2			Y	SCTNR
119951	2002 KX_{14}		39.012	0.04	0.40	4.6			Y	CLSCL
120061	2003 CO_1		20.955	0.48	19.73	9.29	12.93	1.90	N	CENTR
136108	2003 EL_{61}		43.329	0.19	28.21	0.5	–1.23	0.67	Y	SCTNR
136199	2003 UB_{313}	Eris	67.728	0.44	43.97	–1.1	4.48	4.63	Y	SCTNR
136472	2005 FY_9		45.678	0.16	29.00	0.0	10.19	2.25	Y	RESNT
	2002 MS_4		41.560	0.15	17.72	4.0			Y	SCTNR
	2003 AZ_{84}		39.714	0.17	13.52	3.71	1.48	1.01	Y	RESNT

*Small-body number, provisional designation, and proper name for the target sample.

†Orbital semimajor axis (a), eccentricity (e), and inclination (i).

‡Absolute visual magnitude (H_V) and spectral slope and uncertainty (S and σ_S, in % per 100 nm relative to V band), from the photometric literature.

§Orbital semimajor axis > that of Neptune (30.066 AU).

¶Deep Ecliptic Survey dynamical classification (*Elliot et al.,* 2005): CENTR = Centaur, CLSCL = classical, RESNT = resonant, SCTNR = scattered near, SCEXT = scattered extended.

STM gives results and uncertainties that are very similar to those obtained through application of such thermophysical models (e.g., *Stansberry et al.,* 2006). Because the hybrid STM is much simpler, and it produces results comparable to thermophysical models, we employ only the hybrid STM. (We note that thermophysical models are of significant interest for objects where the pole orientation and rotational period of the target are known, because such models can then constrain the thermal inertia, which is of interest in its own right.)

3. SPITZER OBSERVATIONS

Roughly 310 hours of time on the Spitzer have been allocated to attempts to detect thermal emission from KBOs and Centaurs, with the goal of measuring their albedos and diameters. Spitzer has a complement of three instruments, providing imaging capability from 3.6–160 μm, and low-resolution spectroscopy from 5 to 100 μm (*Werner et al.,* 2004). The long-wavelength imager, MIPS (Multiband Imaging Photometer for Spitzer) (*Rieke et al.,* 2004), has 24-, 70-, and 160-μm channels. Because of the placement of these channels, and the sensitivity of the arrays (which are at least 10× more sensitive than previous far-infrared satellites such as IRAS and ISO), MIPS is well suited to studying the thermal emission from KBOs.

3.1. The Sample

Spitzer has targeted over 70 KBOs and Centaurs with MIPS. About two-thirds of the observations have been successful at detecting the thermal emission of the target, although in some of those cases the detections have a low signal-to-noise ratio (SNR). Here we describe observations of 47 KBOs and Centaurs made during the first 3 years of the mission, focusing on observations of the intrinsically brightest objects (i.e., those with the smallest absolute magnitudes, H_V) and the Centaur objects. Table 1 summarizes the orbital and photometric properties of the sample.

The distribution of the objects in terms of dynamical class is also given, in two forms. The second to last column, labeled "TNO?," indicates whether the orbital semimajor axis is larger than Neptune's. By that measure, 31 of the objects are TNOs, and 17 are what might classically be called Centaur objects; that classification is nominally in agreement with the classification scheme proposed in the chapter by Gladman et al., although they classify Okyrhoe and Echeclus as Jupiter-family comets, rather than Centaurs. Another classification scheme has been proposed by *Elliot et al.* (2005) as a part of the Deep Ecliptic Survey (DES) study, and the target classification there under appears as the last column in Table 1. According to the DES classification, 21 of the targets in the Spitzer sample are Centaurs.

Thus, about 30–40% of the sample we discuss here are Centaurs, and the rest are KBOs. Among the KBOs, only 4 objects are classical, while 12 are in mean-motion resonances with Neptune, 9 are in the scattered disk, and one (90377 Sedna) is in the extended scattered disk: Classical objects are underrepresented. Because classical objects do not approach the Sun as closely as the resonant and scattered disk objects, and because they have somewhat fainter absolute magnitudes, the classical objects are at the edge of Spitzer capabilities. One Spitzer program has specifically targeted 15 of the classical objects, but data analysis is ongoing.

The visible photometric properties of the sample are diverse, and generally span the range of observed variation except in terms of the absolute magnitudes, which for the KBOs are generally $H_V \leq 7$. The spectral properties of KBOs and Centaurs are reviewed in the chapters by Barucci et al., Tegler et al., and Doressoundiram et al.: Here we summarize those characteristics as regards our sample. The visible colors, given in Table 1 as the spectral slope (measured relative to V), cover the range from neutral to very red (Pholus). Visible absorption features have been reported in the 0.6–0.75-μm region for 47932 (2000 GN_{171}), 38628 Huya, and (2003 AZ_{84}) (*Lazzarin et al.,* 2003; *de Bergh et al.,* 2004; *Fornasier et al.,* 2004). Several of the targets exhibit near-IR spectral features, with water and methane ices being the dominant absorbers identified. Water ice detections have been made for 10199 Chariklo, 83982 (2002 GO_9), 47171 (1999 TC_{36}), 47932 (2000 GN_{171}), 90482 Orcus, 50000 Quaoar, and 136108 (2003 EL_{61}). 55638 (2002 VE_{95}) exhibits methanol absorption, as does 5145 Pholus, along with its strong water ice absorption. Methane ice is clearly present on Eris (*Brown et al.,* 2005), and 136472 (2005 FY_9) (*Licandro et al.,* 2006a; *Tegler et al.,* 2007; *Brown et al.,* 2007), and Eris may also have N_2 ice (*Licandro et al.,* 2006b). Two of the objects exhibit surface heterogeneity: 31824 Elatus (*Bauer et al.,* 2003) and 32532 Thereus (*Barucci et al.,* 2002; *Merlin et al.,* 2005).

3.2. The Observations

Most of the targets in the sample presented here were observed in both the 24- and 70-μm channels of MIPS. In a few cases, when the target was predicted to be too faint to observe in the second channel, only one channel was used. Integration times vary significantly, ranging from 200–4000 s. As Spitzer observations of KBOs and Centaurs proceeded, it became clear that they were significantly harder to detect than had been predicted prior to the launch. The difficulty was due to a combination of worse-than-predicted sensitivity for the 70-μm array (by a factor of about 2), and the fact that KBOs are colder and smaller than assumed. As these realities made themselves evident, later observing programs implemented more aggressive observing strategies, and have generally been more successful than the early observations.

In some cases the same target was observed more than once. These observations fall into three categories: (1) repeat observations seeking to achieve higher sensitivity [e.g., 15875 (1996 TP_{66}) and 28978 Ixion], (2) multiple visits to characterize lightcurves [20000 Varuna and 47932 (2000 GN_{171}) are the only cases, and neither observation produced a measurable lightcurve], and (3) multiple visits to allow for the subtraction of background objects (so-called "shadow

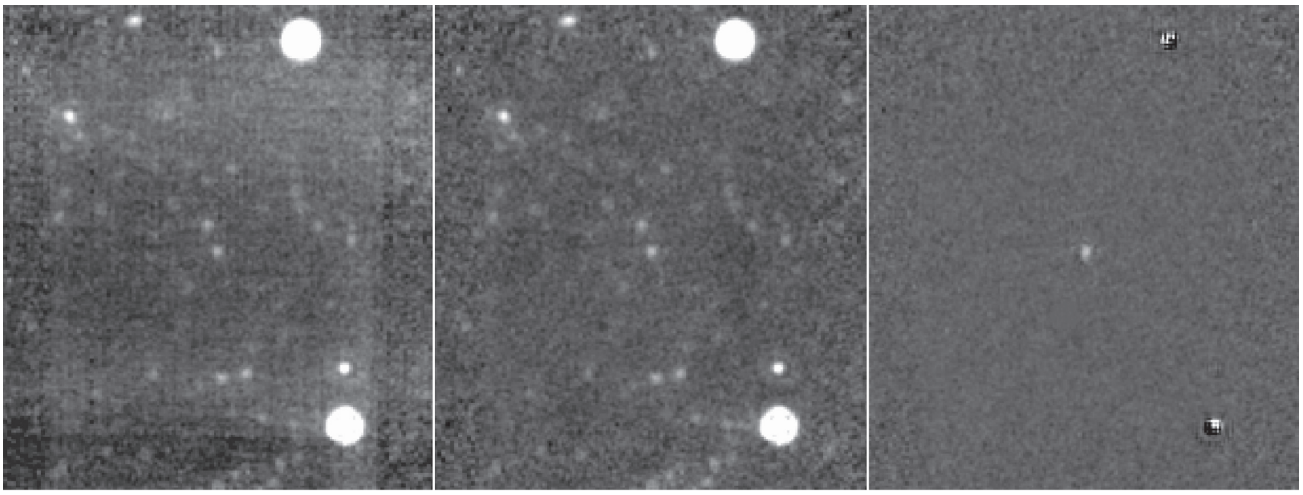

Fig. 2. Processing of the Spitzer 24-μm data for 90482 Orcus. The left panel shows the typical quality of image available through the data pipeline, with scattered light and dark latent artifacts still present. The center panel shows the improvements that can be made by correcting the aforementioned artifacts, and reflects the quality of the data we analyzed for targets that were imaged only once. The right panel shows further improvement due to the subtraction of a shadow observation, and reflects the quality of data we analyzed for targets that were imaged two or more times.

observations"). The basic idea of a shadow observation is to observe the target, wait for it to move out of the way, then re-observe the field. By subtracting the two images, the emission from stationary sources is removed. Figure 2 illustrates the shadow method, as well as some of the extra processing we apply to the Spitzer 24-μm data to improve its quality.

3.3. Photometry

Flux densities were measured using aperture photometry, as described in *Cruikshank et al.* (2005) and *Stansberry et al.* (2006). The apertures used encompassed the core of the PSF, out to about the first Airy minimum (their angular radii were 10" and 15" at 24 and 70 μm). Small apertures were used to maximize the signal-to-noise ratio (SNR) of the measurements. Sky measurements were made in the standard way, with an annulus surrounding the object aperture, and also by placing multiple circular apertures in the region around the target when the presence of background sources or cirrus structure dictated. The photometry was aperture corrected as described in *Engelbracht et al.* (2007) and *Gordon et al.* (2007). Finally, we apply color corrections to our measurements as described in *Stansberry et al.* (2007), resulting in monochromatic flux densities at the effective wavelengths of the 24- and 70-μm filters (23.68 and 71.42 μm, respectively). The MIPS calibration is defined in such a way that the color corrections for stellar spectra are unity. Even though our targets are much colder (typically at or below 80 K), the ≃20% passbands of the MIPS filters result in color corrections that are typically less than 10%.

Uncertainties on the absolute calibration of MIPS are 4% and 5% at 24 and 70 μm, respectively (*Engelbracht et al.,* 2007; *Gordon et al.,* 2007). In our photometry of KBOs and Centaurs we adopt systematic uncertainties of 5% and 10%, to account for the absolute calibration uncertainty and additional uncertainties that may be present, e.g., in our aperture and color corrections. At 70 μm our adopted systematic uncertainty includes significant margin to account for degraded repeatability for faint sources. Additional uncertainty comes from the finite SNR of the detections themselves, which is estimated from the statistics of values falling in the sky annulus and/or sky apertures. We root-sum-square combine the systematic uncertainty with the measurement uncertainty determined from the images to estimate the final error bars on our measurements, and use those total uncertainties in estimating the physical parameters we report. The SNR values we tabulate below reflect the errors estimated from the images, and so reflect the statistical significance of each detection.

4. SPITZER RESULTS

Our flux density measurements, and the albedos and diameters we derive from them, are given in Tables 2 and 3. Table 2 gives our results for those objects observed in both the 24- and 70-μm channel. When only an upper limit on the flux density was achieved, the results in Table 2 bound the albedo and diameter of the target. Table 3 gives the results for those objects observed at only one wavelength, and gives a second interpretation of the data for those objects in Table 2 that were only *detected* at one wavelength.

In both Tables 2 and 3 we give the color corrected flux density of each target, the SNR of the detections, and the temperature we used to perform the color corrections. Where we did not detect the source, we give the 3σ upper limit on the flux density, and the SNR column is blank. When an object was not observed in one of the bands (Table 3 only), the flux and SNR columns are blank. In both Table 2 and 3, albedos (p_V), diameters (D), and beaming parameters (η) follow the fluxes and temperatures.

TABLE 2. Two-band thermal model results.

Number*	Name (Designation)*	AORKEY†	$R_\odot$‡	Δ‡	F_{24}§	SNR_{24}§	F_{70}§	SNR_{70}§	$T_{24:70}$¶	p_V (%)**	D**	η**
29P	Schwassmann-Wachmann 1	7864064	5.734	5.561	253.783	48.0	96.1	18.6	164.7¶	$4.61^{+5.22}_{-1.90}$	$37.3^{-11.8}_{+11.3}$	$0.26^{-0.18}_{+0.28}$
2060	Chiron (1977 UB)	9033216	13.462	13.239	54.410	99.0	145.2	23.4	98.1	$7.57^{+1.03}_{-0.87}$	$233.3^{-14.4}_{+14.7}$	$1.13^{-0.13}_{+0.14}$
5145	Pholus (1992 AD)	9040896	18.614	18.152	3.080	66.0	<19.8		>80.2	$>6.56^{+6.38}_{-2.53}$	$<154.5^{-44.5}_{+42.6}$	$<1.37^{-0.48}_{+0.46}$
5145	Pholus (1992 AD)	12661760	19.827	19.768	0.962	18.8	<10.1		>72.9	$>8.12^{+7.93}_{-3.17}$	$<138.9^{-40.1}_{+38.9}$	$<1.78^{-0.60}_{+0.57}$
8405	Asbolus (1995 GO)	9039360	7.743	7.240	202.394	99.0	155.7	23.6	141.8¶	$5.30^{+1.91}_{-1.25}$	$85.4^{-12.2}_{+12.2}$	$0.66^{-0.20}_{+0.23}$
8405	Asbolus (1995 GO)	12660480	8.748	8.388	73.814	99.0	82.7	11.9	127.4	$5.59^{+1.69}_{-1.17}$	$83.2^{-10.3}_{+10.4}$	$0.93^{-0.22}_{+0.25}$
10199	Chariklo (1997 CU_{26})	8806144	13.075	12.684	78.700	99.0	202.5	24.6	99.1	$5.63^{+0.76}_{-0.65}$	$260.9^{-16.0}_{+16.4}$	$1.17^{-0.13}_{+0.14}$
10199	Chariklo (1997 CU_{26})	9038592	13.165	12.890	61.509	99.0	177.0	40.4	96.3	$5.81^{+0.62}_{-0.55}$	$256.8^{-12.8}_{+13.2}$	$1.29^{-0.12}_{+0.13}$
10370	Hylonome (1995 DW_2)	9038080	19.963	19.824	0.503	14.9	<10.2		>65.0	$>1.07^{+1.04}_{-0.42}$	$<168.4^{-48.5}_{+47.3}$	$<2.89^{-0.84}_{+0.80}$
15820	(1994 TB)	9042688	28.562	28.320	<0.062		<11.1		48.2	$>0.55^{+0.64}_{-0.26}$	$<451.3^{-145.4}_{+176.1}$	$4.87^{-1.47}_{+1.90}$
15874	(1996 TL_{66})	9035776	35.125	34.604	0.380	13.5	22.0	4.4	55.6	$3.50^{+1.96}_{-1.07}$	$575.0^{-114.6}_{+115.5}$	$1.76^{-0.33}_{+0.33}$
15875	(1996 TP_{66})	8805632	26.491	26.250	0.689	17.9	<17.6		>62.7	$>1.97^{+1.88}_{-0.76}$	$<310.9^{-88.7}_{+86.1}$	$<1.89^{-0.53}_{+0.50}$
15875	(1996 TP_{66})	12659456	26.629	26.113	0.426	14.6	<6.9		>67.5	$>6.49^{+6.34}_{-2.54}$	$<171.2^{-49.4}_{+48.3}$	$<1.36^{-0.43}_{+0.41}$
20000	Varuna (2000 WR_{106})	9045760	43.209	42.830	<0.086		11.0	4.9	<50.1	$<11.60^{+7.66}_{-4.59}$	$>621.2^{-139.1}_{+178.1}$	$>1.73^{-0.46}_{+0.63}$
26308	(1998 SM_{165})	14402560	36.417	36.087	0.105	15.9	5.2	9.4	56.8	$6.33^{+1.53}_{-1.16}$	$279.8^{-28.6}_{+29.7}$	$1.48^{-0.17}_{+0.17}$
26375	(1999 DE_9)	9047552	34.980	34.468	0.905	38.2	22.6	9.3	62.9	$6.85^{+1.58}_{-1.19}$	$461.0^{-45.3}_{+46.1}$	$1.05^{-0.12}_{+0.12}$
28978	Ixion (2001 KX_{76})	9033472	42.731	42.448	0.584	16.6	19.6	3.5	60.1	$15.65^{+12.00}_{-5.53}$	$573.1^{-141.9}_{+139.7}$	$0.82^{-0.22}_{+0.21}$
28978	Ixion (2001 KX_{76})	12659712	42.510	42.058	0.290	7.9	<18.4		>54.9	$>12.03^{+12.08}_{-4.89}$	$<653.6^{-191.9}_{+194.6}$	$<1.22^{-0.37}_{+0.36}$
29981	(1999 TD_{10})	8805376	14.137	13.945	4.629	31.6	19.5	7.2	87.9	$4.40^{+1.42}_{-0.96}$	$103.7^{-13.5}_{+13.6}$	$1.64^{-0.31}_{+0.32}$
31824	Elatus (1999 UG_5)	9043200	10.333	9.998	6.015	69.8	<12.4		>105.2	$>4.86^{+5.17}_{-1.95}$	$<47.4^{-14.4}_{+13.8}$	$<1.46^{-0.66}_{+0.68}$
31824	Elatus (1999 UG_5)	12661248	11.125	10.826	8.596	99.0	<8.9		>118.3¶	$>9.41^{+11.57}_{-3.97}$	$<34.1^{-11.3}_{+10.8}$	$<0.50^{-0.29}_{+0.33}$
32532	Thereus (2001 PT_{13})	9044480	9.813	9.357	25.938	99.0	32.7	4.8	122.3	$8.93^{+5.35}_{-2.79}$	$60.8^{-12.7}_{+12.5}$	$0.86^{-0.32}_{+0.35}$
32532	Thereus (2001 PT_{13})	12660224	9.963	9.685	23.722	99.0	46.8	10.3	106.5	$4.28^{+1.09}_{-0.80}$	$87.8^{-9.4}_{+9.5}$	$1.50^{-0.28}_{+0.30}$
38628	Huya (2000 EB_{173})	8808192	29.326	29.250	3.630	69.4	57.2	10.9	67.9	$4.78^{+0.94}_{-0.74}$	$546.5^{-47.1}_{+47.8}$	$1.10^{-0.11}_{+0.12}$
38628	Huya (2000 EB_{173})	8937216	29.325	29.210	3.400	69.0	52.9	28.4	68.0	$5.22^{+0.47}_{-0.43}$	$523.1^{-21.9}_{+22.7}$	$1.09^{-0.07}_{+0.07}$
47171	(1999 TC_{36})	9039104	31.098	30.944	1.233	56.4	25.3	10.0	64.9	$7.18^{+1.53}_{-1.17}$	$414.6^{-38.2}_{+38.8}$	$1.17^{-0.12}_{+0.13}$
47932	(2000 GN_{171})	9027840	28.504	28.009	0.258	8.2	11.9	5.6	57.4	$5.68^{+2.54}_{-1.59}$	$321.0^{-54.2}_{+57.4}$	$2.32^{-0.43}_{+0.46}$
50000	Quaoar (2002 LM_{60})	10676480	43.345	42.974	0.279	5.5	24.6	4.2	52.5	$19.86^{+13.17}_{-7.04}$	$844.4^{-189.6}_{+206.7}$	$1.37^{-0.36}_{+0.39}$
52872	Okyrhoe (1998 SG_{35})	8807424	7.793	7.405	28.767	99.0	37.4	9.1	121.0	$2.49^{+0.81}_{-0.55}$	$52.1^{-6.9}_{+6.9}$	$1.46^{-0.35}_{+0.39}$
54598	Bienor (2000 QC_{243})	9041920	18.816	18.350	3.528	78.0	29.7	6.1	76.0	$3.44^{+1.27}_{-0.82}$	$206.7^{-30.1}_{+30.1}$	$1.69^{-0.30}_{+0.30}$
55565	(2002 AW_{197})	9043712	47.131	46.701	0.155	7.7	15.0	6.7	51.9	$11.77^{+4.42}_{-3.00}$	$734.6^{-108.3}_{+116.4}$	$1.26^{-0.20}_{+0.22}$
55576	Amycus (2002 GB_{10})	17766144	15.589	15.155	6.367	86.1	13.6	5.8	99.9¶	$17.96^{+7.77}_{-4.70}$	$76.3^{-12.5}_{+12.5}$	$0.64^{-0.18}_{+0.19}$
55636	(2002 TX_{300})	10676992	40.979	40.729	<0.065		<11.1		48.4	$>17.26^{+20.33}_{-8.33}$	$<641.2^{-206.7}_{+250.3}$	$2.16^{-0.78}_{+0.95}$
55637	(2002 UX_{25})	10677504	42.368	42.413	0.486	15.0	23.0	5.3	57.2	$11.50^{+5.09}_{-3.09}$	$681.2^{-114.0}_{+115.6}$	$1.04^{-0.18}_{+0.18}$
60558	Echeclus (2000 EC_{98})	8808960	14.141	13.736	4.901	84.7	15.5	5.0	94.0	$3.83^{+1.89}_{-1.08}$	$83.6^{-15.2}_{+15.0}$	$1.25^{-0.32}_{+0.33}$
65489	Ceto (2003 FX_{128})	17763840	27.991	27.674	1.463	71.5	14.6	12.2	73.6	$7.67^{+1.38}_{-1.10}$	$229.7^{-18.2}_{+18.6}$	$0.86^{-0.09}_{+0.10}$
73480	(2002 PN_{34})	17762816	14.608	14.153	10.368	99.0	31.0	12.6	95.3	$4.25^{+0.83}_{-0.65}$	$119.5^{-10.2}_{+10.3}$	$1.10^{-0.15}_{+0.16}$

TABLE 2. (continued).

Number*	Name (Designation)*	AORKEY†	$R_\odot$‡	Δ‡	F_{24}§	SNR_{24}§	F_{70}§	SNR_{70}§	$T_{24:70}$¶	p_V (%)**	D**	η**
83982	Crantor (2002 GO_9)	9044224	14.319	13.824	2.276	58.6	<8.7		>89.8	$>8.60^{+8.62}_{-3.36}$	$<66.7^{-19.6}_{+18.7}$	$<1.44^{-0.57}_{+0.56}$
84522	(2002 TC_{302})	13126912	47.741	47.654	0.054	6.5	18.0	3.1	44.8	$3.08^{+2.93}_{-1.24}$	$1145.4^{-325.0}_{+337.4}$	$2.33^{-0.54}_{+0.53}$
84922	(2003 VS_2)	10680064	36.430	36.527	0.304	6.0	25.7	3.5	52.8	$5.84^{+4.78}_{-2.24}$	$725.2^{-187.6}_{+199.0}$	$2.00^{-0.51}_{+0.54}$
90482	Orcus (2004 DW)	13000448	47.677	47.442	0.329	32.4	26.6	12.5	53.1	$19.72^{+3.40}_{-2.76}$	$946.3^{-72.3}_{+74.1}$	$1.08^{-0.09}_{+0.10}$
90568	(2004 GV_9)	13000960	38.992	39.007	0.166	18.2	17.5	9.2	51.4	$8.05^{+1.94}_{-1.46}$	$677.2^{-69.3}_{+71.3}$	$1.94^{-0.20}_{+0.20}$
119951	(2002 KX_{14})	10678016	39.585	39.197	<0.109		<11.7		51.2	$>8.09^{+9.58}_{-3.91}$	$<561.6^{-181.5}_{+219.9}$	$1.91^{-0.66}_{+0.84}$
120061	(2003 CO_1)	17764864	10.927	10.917	21.722	99.0	33.4	11.3	114.7	$5.74^{+1.49}_{-1.09}$	$76.9^{-8.4}_{+8.5}$	$0.91^{-0.18}_{+0.20}$
136108	(2003 EL_{61})††	13803008	51.244	50.920	<0.022		7.8	5.3	<44.6	?‡‡	?‡‡	?‡‡
136199	Eris (2003 UB_{313})††	15909632	96.907	96.411	<0.014		2.7	4.0	<40.1	?‡‡	?‡‡	?‡‡
136472	(2005 FY_9)††	13803776	51.884	51.879	0.296	21.1	14.6	9.4	54.8	?‡‡	?‡‡	?‡‡
	(2002 MS_4)	10678528	47.402	47.488	0.391	20.5	20.0	5.1	56.6	$8.41^{+3.78}_{-2.26}$	$726.2^{-122.9}_{+123.2}$	$0.88^{-0.15}_{+0.14}$
	(2003 AZ_{84})	10679040	45.669	45.218	0.291	12.4	17.8	6.7	55.2	$12.32^{+4.31}_{-2.91}$	$685.8^{-95.5}_{+98.8}$	$1.04^{-0.16}_{+0.16}$

*Small-body number, provisional designation, and proper name for the target sample.

†Unique key identifying the data in the Spitzer data archive.

‡Target distance from the Sun and Spitzer, in AU.

§Color-corrected flux densities (mJy) at 23.68 μm and 71.42 μm. Upper limits are 3σ. SNR is signal-to-noise ratio in the images (see text).

¶The temperature of the blackbody spectrum used to compute the color correction. In most cases this is the 24:70-μm color temperature, but for the four denoted targets, the subsolar blackbody temperature was lower than the color temperature, and we used that instead.

**The visible geometric albedo (p_V, percentage), diameter (D, km), and beaming parameter (η) from hybrid STM fits. Fits to upper limits provide a quantitative interpretation of the constraints they place on p_V and D.

††Results for 136199 Eris, 136199 (2003 EL_{61}), and 136472 (2005 FY_9) assumed a phase integral of 0.8, typical of Pluto.

‡‡No STM with plausible albedo and beaming parameter can simultaneously fit the 24- and 70-μm data. For 136472, models with two albedo terrains can fit the data, and give D ≃ 1500 km.

TABLE 3. Single-band thermal model results.

Number*	Name (Designation)*	AORKEY*	$R_\odot$*	Δ*	F_{24}*	SNR_{24}*	F_{70}*	SNR_{70}*	T_{SS}†	KBO-Tuned STM		p_V‡ (%)	D‡
										p_V (%)‡	D‡	STM_0 ILM_0	STM_0 ILM_0
5145	Pholus (1992 AD)	9040896	18.614	18.152	3.119	66.0	<19.6		91.4	$8.16^{+6.16}_{-?}$	$138.6^{-34.0}_{+?}$	17.07–?	95.8–?
5145	Pholus (1992 AD)	12661760	19.827	19.768	0.987	18.8	<10.0		88.6	$16.18^{+11.55}_{-5.88}$	$98.4^{-23.2}_{+25.0}$	32.74–?	69.2–?
7066	Nessus (1993 HA_2)	9033984	19.501	19.219	0.440	12.4			89.3	$6.53^{+5.14}_{-2.46}$	$59.7^{-15.1}_{+15.9}$	14.02–1.44	40.8–127.4
10370	Hylonome (1995 DW_2)	9038080	19.963	19.824	0.530	14.9	<10.0		88.3	$6.12^{+4.91}_{-2.33}$	$70.5^{-18.0}_{+19.1}$	13.28–1.32	47.9–152.0
10370	Hylonome (1995 DW_2)	12659968	20.333	20.390	0.451	16.0			87.5	$6.33^{+5.12}_{-2.42}$	$69.3^{-17.8}_{+18.9}$	13.80–1.34	46.9–150.5
15875	(1996 TP_{66})	8805632	26.491	26.250	0.720	17.9	<17.3		76.6	$5.17^{+4.98}_{-2.19}$	$191.8^{-54.9}_{+60.9}$	12.54–?	123.1–?
15875	(1996 TP_{66})	12659456	26.629	26.113	0.437	14.6	<6.8		76.4	$8.21^{+7.61}_{-?}$	$152.2^{-42.6}_{+?}$	19.37–?	99.1–?
20000	Varuna (2000 WR_{106})	9045760	43.209	42.830	<0.094		10.9	4.9	60.0	?	?	?–8.09	?–744.1
20000	Varuna (2000 WR_{106})	9031680	43.261	43.030			10.0	5.6	60.0	$17.77^{+6.17}_{-3.79}$	$502.0^{-69.5}_{+64.0}$	26.34–8.68	412.3–718.2
28978	Ixion (2001 KX_{76})	12659712	42.510	42.058	0.303	7.9	<18.3		60.5	25.81§	446.3§	32.28–?	399.1–?
31824	Elatus (1999 UG_5)	9043200	10.333	9.998	5.990	69.8	<12.3		122.7	$6.41^{+3.52}_{-?}$	$41.3^{-8.1}_{+?}$	11.41–?	31.0–?
31824	Elatus (1999 UG_5)	12661248	11.125	10.826	8.596	99.0	<8.9		118.3	?	?	?–?	?–?
35671	(1998 SN_{165})	9040384	37.967	37.542			14.7	6.3	64.0	$4.33^{+1.50}_{-0.91}$	$458.2^{-63.1}_{+57.1}$	6.42–2.17	376.4–648.1
42355	Typhon (2002 CR_{46})	9029120	17.581	17.675			31.4	8.6	94.1	$5.09^{+1.24}_{-0.80}$	$173.8^{-18.0}_{+15.6}$	6.81–3.13	150.3–221.7
52975	Cyllarus (1998 TF_{35})	9046528	21.277	21.001	0.274	8.7			85.5	$11.46^{+8.96}_{-4.36}$	$61.9^{-15.5}_{+16.8}$	24.43–2.42	42.4–134.9
63252	(2001 BL_{41})	9032960	9.856	9.850	4.864	95.6			125.7	$3.90^{+2.12}_{-1.14}$	$34.2^{-6.7}_{+6.5}$	6.93–1.34	25.6–58.3
83982	Crantor (2002 GO_9)	9044224	14.319	13.824	2.310	58.6	<8.6		104.2	$11.18^{+7.09}_{-?}$	$58.5^{-12.7}_{+?}$	21.28–?	42.4–?
90377	Sedna (2003 VB_{12})¶,**	8804608	89.527	89.291			<2.4		41.7	$>20.91^{+8.71}_{-5.29}$	$<1268.8^{-202.7}_{+199.4}$	32.93–8.17	1010.9–2029.0
136108	(2003 EL_{61})¶	13803008	51.244	50.920	<0.025		7.7	5.3	55.1	$84.11^{+9.48}_{-8.10}$	$1151.0^{-59.9}_{+59.8}$	96.41–59.12	1075.1–1372.9
136199	Eris (2003 UB_{313})¶	15909632	96.907	96.411	<0.014		2.7	4.0	40.1	$68.91^{+12.24}_{-9.98}$	$2657.0^{-208.6}_{+216.1}$	84.90–39.17	2393.7–3523.9
136472	(2005 FY_9)¶	13803776	51.884	51.879	††		14.6	9.4	54.8	$78.20^{+10.30}_{-8.55}$	$1502.9^{-90.2}_{+89.6}$	91.63–52.55	1388.3–1833.3
136472	(2005 FY_9)¶	13803776	51.884	51.879	0.296	21.1	††		54.8	$35.99^{+17.56}_{-12.25}$	$2215.2^{-399.2}_{+512.4}$	59.34–6.27	1725.3–5307.0

*The first nine columns are identical to those in Table 2. Flux densities that are blank indicate no data exist.

†The subsolar temperature of a blackbody at the distance of the target. Color corrections are made using a blackbody spectrum with this temperature.

‡The range of visible geometric albedos (given as a percentage) and diameter (in km) derived from fitting the KBO-tuned STM (i.e., $\eta = 1.2 \pm 0.35$) and the canonical STM and ILM. "?" indicates the model emission violates a flux limit.

§Only the KBO-tuned STM using $\eta = 0.85$ did not violate the 70-μm flux limit for this observation of Ixion.

¶Results for 90377 Sedna, 136108 (2003 EL_{61}), Eris, and 136472 (2005 FY_9) assumed a phase integral of 0.8, typical of Pluto.

**Fit to the 70-μm upper limit: lower bound on p_V, upper bound on D.

††Fits to the individual bands for 136472 (2005 FY_9) are shown; it is not possible to simultaneously fit both bands with a single thermal model.

4.1. Two-Wavelength Results

As discussed earlier and demonstrated in Fig. 1, the model-dependent uncertainties in the albedo and diameter we derive for targets detected at both 24 and 70 μm are much smaller than those uncertainties for objects detected in only one of those bands, and in particular are usually very much smaller than for objects detected only at 24 μm. For this reason, we focus first on the targets we either detected at both wavelengths, or for which we have constraints on the flux density at both. We use these results to inform our models for targets with single-band detections and limits.

We apply the hybrid STM to the observed flux densities as follows. For targets *detected* in both bands (Table 2), we fit the observed flux densities and the 1σ error bars, deriving albedo and diameter values and 1σ uncertainties on them. For those objects with an *upper limit* in one band and a detection in the other, we fit the detection and the the upper limit in order to quantitatively interpret the constraints the limit implies for the albedo and diameter. For this second class of observation, we also perform a single-wavelength analysis (see Table 3) in order to derive independent constraints on these properties. While the results given in Table 2 include values of the beaming parameter, η, those values only reflect the departures of the measured emission from the assumptions of the STM; had we chosen to model the data with the ILM, the fitted values for η would be entirely different (even though p_V and D would be very similar). Results from observations made at very similar epochs are averaged. An exception to that rule is the two observations of 38628 Huya. Those data were analyzed independently to provide a check on the repeatability of our overall data analysis and modeling methods for a "bright" KBO, and show agreement at the 4% level for p_V and at the 2% level for D.

The average behavior of the targets is of particular interest for interpreting single-wavelength observations, where we have no independent means for constraining η. Restricting our attention to those targets detected at SNR ≥ 5 at both 24 and 70 μm, and excluding the highest- and lowest-albedo object from each class, we find that for outer solar system objects the average beaming parameter is $\eta = 1.2 \pm 0.35$. We reexamine the average properties of the sample later.

4.2. Single-Wavelength Results

Because we are primarily interested in the albedos and sizes of our targets, we fit our single-wavelength observations with the STM, setting the beaming parameter to the average value determined above: We term this model the "KBO-tuned" STM. We also apply the canonical STM and ILM (i.e., with $\eta = 0.756$ and 1.0, respectively) to the single-wavelength data, to interpret the data in the context of these endmember models and assess the resulting uncertainties in model parameters.

Table 3 gives the results for the single-wavelength sample, including those objects in Table 2 with a detection at one wavelength and an upper-limit at the other. Where a model violates a flux limit, the corresponding albedo and diameter entries appear as a "?". The albedos and diameters we derive using the average beaming parameter from the two-wavelength sample are in the columns labeled "KBO-Tuned STM"; the range of albedos and diameters resulting from application of the canonical STM and ILM are labeled "STM_0" and "ILM_0". Note that the flux densities for objects in both Table 2 and 3 are sometimes slightly different, because in Table 3 the color correction is based on the blackbody temperature at the object's distance, rather than on the 24:70-μm color temperature.

4.3. Spitzer Albedos and Diameters

The results presented above include low SNR detections, nondetections, and multiple results for some targets. In the top portion of Table 4 we present results for the 39 targets that were detected at SNR ≥ 5 at one or both wavelengths. The results for targets that were visited multiple times are averaged unless one observation shows some indication of a problem. Targets with an upper limit in either band appear in both Tables 2 and 3; in the top portion of Table 4 we give values that are representative of all the earlier models. The top portion of the table contains 39 objects: 26 detected at both 24 and 70 μm, 9 at 24 μm only, and 4 at 70 μm only. Seventeen of the objects have orbital semimajor axes inside Neptune, and 21 exterior to Neptune's orbit. Where other albedo and diameter determinations exist, Table 4 summarizes the result, the basis of the determination, and the publication.

4.4. Other Constraints on p_V and D

The albedos and sizes of about 20 TNOs and several Centaurs have been determined by other groups using various methods; the lower portion of Table 4 presents those results not given in the top portion of the table, and the constraints that can be derived from Spitzer data, when those exist (although the SNR for all five cases is low, and for 90377 Sedna only a 70-μm limit is available).

In general our results and those of other groups agree at the ≤2σ level [e.g., 10199 Chariklo, 26308 (1998 SM_{165}), 47171 (1999 TC_{36}), 55565 (2002 AW_{197}), 136199 Eris, 136108 (2003 EL_{62})]. In a few cases there are discrepancies. For example, our results for 20000 Varuna are inconsistent with the millimeter results of *Jewitt et al.* (2001) and *Lellouch et al.* (2002), which suggest a significantly larger size and lower albedo. While our detection at 70 μm nominally satisfied the 5σ threshold for Table 4, the background showed significant structure and the SNR of the detection in the individual visits was actually quite low. Combined with the fact that we were not able to directly fit the beaming parameter, we are inclined to favor the submillimeter results for this object over those from Spitzer. While there is some tendency for the Spitzer diameters to be smaller and albedos higher, there is generally good agreement be-

TABLE 4. Adopted physical properties.

		Physical Properties from Spitzer Data					Other Methods			
Number*	Name (Designation)*	p_V*	D*	η*	λ_{detect}†	TNO?*	Method‡	p_V*	D*	Reference§
29P	Schwassmann-Wachmann	$14.61^{+5.22}_{-1.90}$	$37.3^{-11.8}_{+11.3}$	$0.26^{-0.18}_{+0.28}$	both	Cen	mIR	13 ± 4	40 ± 5	Cr83
2060	Chiron (1977 UB)	$7.57^{+1.03}_{-0.87}$	$233.3^{-14.4}_{+14.7}$	$1.13^{-0.13}_{+0.14}$	both	Cen	mIR	17 ± 2	144 ± 8	Fe02
							ISO	11 ± 2	142 ± 10	Gn04
							mIR	14 ± 5	180	Ca94
5145	Pholus (1992 AD)	8.0^{+7}_{-3}	140^{-40}_{+40}	$1.3^{-0.4}_{+0.4}$	24	Cen	mIR	4.4 ± 1.3	189 ± 26	Da93
							IRS	7.2 ± 2	148 ± 25	Cr06
7066	Nessus (1993 HA_2)	$6.5^{+5.3}_{-2.5}$	60^{-16}_{+16}	$1.2^{-0.35}_{+0.35}$	24	Cen				
8405	Asbolus (1995 GO)	$5.46^{+1.27}_{-0.86}$	$84.2^{-7.8}_{+7.8}$	$0.80^{-0.16}_{+0.17}$	both	Cen	mIR	12 ± 3	66 ± 4	Fe02
							IRS	4.3 ± 1.4	95 ± 7	Cr06
10199	Chariklo (1997 CU_{26})	$5.73^{+0.49}_{-0.42}$	$258.6^{-10.3}_{+10.3}$	$1.23^{-0.09}_{+0.10}$	both	Cen	mm	5.5 ± 0.5	275	Al02
							mIR/mm	7 ± 1	246 ± 12	Gn04
10370	Hylonome (1995 DW_2)	6.2^{+5}_{-3}	70^{-20}_{+20}	$1.2^{-0.35}_{+0.35}$	24	Cen				
15875	(1996 TP_{66})	7.4^{+7}_{-3}	160^{-45}_{+45}	$1.2^{-0.35}_{+0.35}$	24	TNO				
20000	Varuna (2000 WR_{106})	16^{+10}_{-8}	500^{-100}_{+100}	$1.2^{-0.35}_{+0.35}$	70	TNO	submm	6 ± 2	1016 ± 156	Je01, Al04
							mm	7 ± 3	914 ± 156	Le02, Al04
26308	(1998 SM_{165})	$6.33^{+1.53}_{-1.16}$	$279.8^{-28.6}_{+29.7}$	$1.48^{-0.17}_{+0.17}$	both	TNO	mm/bin	9.1 ± 4	238 ± 55	Ma04, Gy05
26375	(1999 DE_9)	$6.85^{+1.58}_{-1.19}$	$461.0^{-45.3}_{+46.1}$	$1.05^{-0.12}_{+0.12}$	both	TNO				
28978	Ixion (2001 KX_{76})	12^{+14}_{-6}	650^{-220}_{+260}	$0.8^{-0.2}_{+0.2}$	24	TNO	mm	>15	<804	Al04
29981	(1999 TD_{10})	$4.40^{+1.42}_{-0.96}$	$103.7^{-13.5}_{+13.6}$	$1.64^{-0.31}_{+0.32}$	both	TNO	IRS	6.5	98	Cr06
31824	Elatus (1999 UG_5)	10^{+4}_{-3}	30^{-8}_{+8}	$1.2^{-0.35}_{+0.35}$	24	Cen	IRS	5.7 ± 2	36 ± 8	Cr06
32532	Thereus (2001 PT_{13})	$4.28^{+1.09}_{-0.80}$	$87.8^{-9.4}_{+9.5}$	$1.50^{-0.28}_{+0.30}$	both	Cen				
35671	(1998 SN_{165})	$4.3^{+1.8}_{-1.2}$	460^{-80}_{+60}	$1.2^{-0.35}_{+0.35}$	70	TNO				
38628	Huya (2000 EB_{173})	$5.04^{+0.50}_{-0.41}$	$532.6^{-24.4}_{+25.1}$	$1.09^{-0.06}_{+0.07}$	both	TNO	mm	>8	<540	Al04
42355	Typhon (2002 CR_{46})	$5.1^{+1.3}_{-0.9}$	175^{-20}_{+17}	$1.2^{-0.35}_{+0.35}$	70	TNO				
47171	(1999 TC_{36})	$7.18^{+1.53}_{-1.17}$	$414.6^{-38.2}_{+38.8}$	$1.17^{-0.12}_{+0.13}$	both	TNO	mm	5 ± 1	609 ± 70	Al04
							mm/bin	14 ± 6	302 ± 70	Ma04, Gy05
47932	(2000 GN_{171})	$5.68^{+2.54}_{-1.59}$	$321.0^{-54.2}_{+57.4}$	$2.32^{-0.43}_{+0.46}$	both	TNO				
50000	Quaoar (2002 LM_{60})	$19.9^{+13.2}_{-7}$	844^{-190}_{+207}	$1.4^{-0.4}_{+0.4}$	both	TNO	image	9 ± 3	1260 ± 190	Br04
52872	Okyrhoe (1998 SG_{35})	$2.49^{+0.81}_{-0.55}$	$52.1^{-6.9}_{+6.9}$	$1.46^{-0.35}_{+0.39}$	both	Cen				
52975	Cyllarus (1998 TF_{35})	11.5^{+9}_{-5}	62^{-18}_{+20}	$1.2^{-0.35}_{+0.35}$	24	Cen				
54598	Bienor (2000 QC_{243})	$3.44^{+1.27}_{-0.82}$	$206.7^{-30.1}_{+30.1}$	$1.69^{-0.30}_{+0.30}$	both	Cen				
55565	(2002 AW_{197})	$11.77^{+4.42}_{-3.00}$	$734.6^{-108.3}_{+116.4}$	$1.26^{-0.20}_{+0.22}$	both	TNO	mm	9 ± 2	977 ± 130	Ma02
55576	Amycus (2002 GB_{10})	$17.96^{+7.77}_{-4.70}$	$76.3^{-12.5}_{+12.5}$	$0.64^{-0.18}_{+0.19}$	both	Cen				
55637	(2002 UX_{25})	$11.50^{+5.09}_{-3.09}$	$681.2^{-114.0}_{+115.6}$	$1.04^{-0.18}_{+0.18}$	both	TNO				
60558	Echeclus (2000 EC_{98})	$3.83^{+1.89}_{-1.08}$	$83.6^{-15.2}_{+15.0}$	$1.25^{-0.32}_{+0.33}$	both	Cen				
63252	(2001 BL_{41})	$3.9^{+2.5}_{-1.3}$	35^{-8}_{+7}	$1.2^{-0.35}_{+0.35}$	24	Cen				

TABLE 4. (continued).

		Physical Properties from Spitzer Data					Other Methods			
Number*	Name (Designation)*	p_V*	D*	η*	λ_{detect}†	TNO?*	Method‡	p_V*	D*	Reference§
65489	Ceto (2003 FX_{128})	$7.67^{+1.38}_{-1.10}$	$229.7^{-18.2}_{+18.6}$	$0.86^{-0.09}_{+0.10}$	both	TNO				
73480	(2002 PN_{34})	$4.25^{+0.83}_{-0.65}$	$119.5^{-10.2}_{+10.3}$	$1.1^{-0.15}_{+0.16}$	both	TNO				
83982	Crantor (2002 GO_9)	11^{+7}_{-4}	60^{-13}_{+15}	$1.20^{-0.35}_{+0.35}$	24	Cen				
90482	Orcus (2004 DW)	$19.72^{+3.40}_{-2.76}$	$946.3^{-72.3}_{+74.1}$	$1.08^{-0.09}_{+0.10}$	both	TNO				
90568	(2004 GV_9)	$8.05^{+1.94}_{-1.46}$	$677.2^{-69.3}_{+71.3}$	$1.94^{-0.20}_{+0.20}$	both	TNO				
120061	(2003 CO_1)	$5.74^{+1.49}_{-1.09}$	$76.9^{-8.4}_{+8.5}$	$0.91^{-0.18}_{+0.20}$	both	Cen				
136108	(2003 EL_{61})	$84.^{+10.}_{-20.}$	$1150.^{-100}_{+250}$		70	TNO	Lcurve	65 ± 6	1350 ± 100	Ra05
136472	(2005 FY_9)	$80.^{+10.}_{-20.}$	$1500.^{-200}_{+400}$		both	TNO				
	(2002 MS_4)	$8.41^{+3.78}_{-2.26}$	$726.2^{-122.9}_{+123.2}$	$0.88^{-0.15}_{+0.14}$	both	TNO				
	(2003 AZ_{84})	$12.32^{+4.31}_{-2.91}$	$685.8^{-95.5}_{+98.8}$	$1.04^{-0.16}_{+0.16}$	both	TNO				
15789	(1993 SC)					TNO	ISO	3.5 ± 1.4	298 ± 140	Th00
15874	(1996 TL_{66})	$3.5^{+2.0}_{-1.1}$	575^{-115}_{+116}	$1.8^{-0.3}_{+0.3}$	both	TNO	ISO	>1.8	<958	Th00
19308	(1996 TO_{66})					TNO	mm	>3.3	<902	Al04, Gy05
19521	Chaos (1998 WH_{24})					TNO	mm	>5.8	<747	Al04, Gy05
24835	(1995 SM_{55})					TNO	mm	>6.7	<704	Al04, Gy05
55636	(2002 TX_{300})	>10	<800		limit	TNO	mm	>19	<709	Or04, Gy05
58534	(1997 CQ_{29})					TNO	bin	39 ± 17	77 ± 18	Ma04, No04, Gy05
66652	(1999 RZ_{253})					TNO	bin	29 ± 12	170 ± 39	No04, Gy05
84522	(2002 TC_{302})	$3.1^{+2.9}_{-1.2}$	1150^{-325}_{+337}	$2.3^{-0.5}_{+0.5}$	both	TNO	mm	>5.1	<1211	Al04, Gy05
88611	(2001 QT_{297})					TNO	bin	10 ± 4	168 ± 38	Os03, Gy05
90377	Sedna (2003 VB_{12})	>16.	<1600.		limit	TNO	image	>8.5	<1800	Br04a
136199	Eris (2003 UB_{313})	$70.^{+15.}_{-20.}$	$2600.^{-200}_{+400}$		70	TNO	mm	60 ± 8	3000 ± 200	Be06
							image	86 ± 7	2400 ± 100	Br06
	(1998 WW_{31})					TNO	bin	6 ± 2.6	152 ± 35	Ve02, Gy05
	(2001 QC_{298})					TNO	bin	2.5 ± 1.1	244 ± 55	Ma04, Gy05

*Columns 1–5 and 7 are as defined in Table 2.

†Wavelengths where the objects were detected at SNR > 5 (above horizontal line) or have lower quality Spitzer data (below line).

‡Method by which the diameter was measured. bin = binary mass plus density assumption; image = HST upper limit; IRS = Spitzer mid-IR spectra; ISO = Infrared Space Observatory; Lcurve = lightcurve + rotation dynamics; mIR = groundbased 10–20 μm; mm = typically 1.2-mm groundbased data; submm = typically 850-μm groundbased data.

§References: Al02 = *Altenhoff et al.* (2002); Al04 = *Altenhoff et al.* (2004); Be06 = *Bertoldi et al.* (2006); Br04 = *Brown and Trujillo* (2004); Br04a = *Brown et al.* (2004); Br06 = *Brown et al.* (2006); Ca94 = *Campins et al.* (1994); Cr83 = *Cruikshank and Brown* (1983); Cr06 = *Cruikshank et al.* (2006); Da93 = *Davies et al.* (1993); Fe02 = *Fernandez et al.* (2002); Gn04 = *Groussin et al.* (2004); Gy05 = *Grundy et al.* (2005); Je01 = *Jewitt et al.* (2001); Le02 = *Lellouch et al.* (2002); Ma02 = *Margot et al.* (2002); Ma04 = *Margot et al.* (2004); No04 = *Noll et al.* (2004); Or04 = *Ortiz et al.* (2004); Os03 = *Osip et al.* (2003); Ra05 = *Rabinowitz et al.* (2005); Th00 = *Thomas et al.* (2000); Ve02 = *Veillet et al.* (2002).

Results above the horizontal line have Spitzer detections with SNR > 5; those below the line have SNR < 5, or no Spitzer data.

tween our Spitzer results and those from other groups and methods.

5. ALBEDO STATISTICS AND CORRELATIONS

The Kuiper belt is full of complexity, in terms of the dynamical history and the spectral character of its inhabitants. It is natural to look for relationships between the albedos of KBOs and their orbital and other physical parameters. Figure 3 shows the Spitzer albedos for detections with SNR ≥ 5 (top portion of Table 4) as a function of orbital semimajor axis, a, perihelion distance, $q_{\odot}$, object diameter, D, and visible spectral slope, S. Because of their significant intrinsic interest, the data for 136199 (2003 EL_{61}) and 90377 Sedna are also plotted. Immediately apparent in all these plots is the marked distinction between the largest objects [136199 Eris, 136108 (2003 EL_{61}), and 136472 (2005 FY_9)] and the rest of the objects. 90377 Sedna probably also belongs to this class, although our data only place a lower bound on its albedo. Eris and 136472 (2005 FY_9) both have abundant CH_4 ice on their surfaces, and so are expected to have very high albedos. 90377 Sedna's near-IR spectrum also shows evidence for CH_4 and N_2 ices (*Barucci et al.,* 2005; *Emery et al.,* 2007), and *Schaller and Brown* (2007) show that those ices should not be depleted by Jean's escape: It seems likely that 90377 Sedna's albedo is quite high. The surface of 136199 (2003 EL_{61}) is dominated by water-ice absorptions, with no evidence for CH_4 or N_2, yet also has a very high albedo. Charon, which has a similar spectrum, has $p_V \simeq 37\%$, but some saturnian satellites (notably Enceladus and Tethys) have albedos ≥ 80% (*Morrison et al.,* 1986).

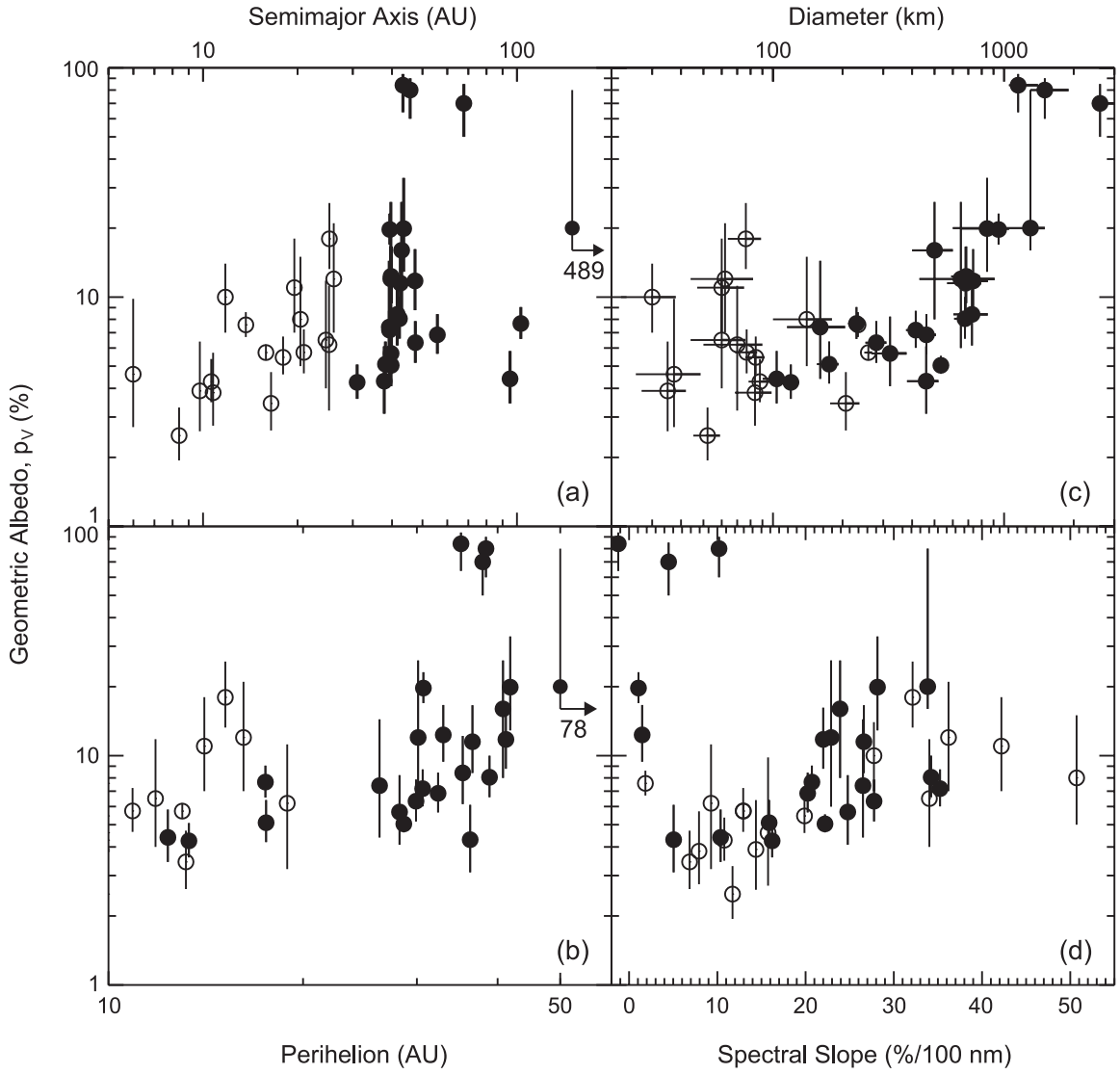

Fig. 3. Geometric albedo plotted vs. **(a)** orbital semimajor axis, **(b)** orbital perihelion distance, **(c)** object diameter, and **(d)** the slope of the object's visible spectrum (i.e., color). Open circles are for Centaur objects (a < 30.066 AU); filled circles are for TNOs. In **(a)** the point for 90377 Sedna has been plotted at a = 150 AU rather than at its true semimajor axis of 489 AU. In **(b)** the point for 90377 Sedna has been plotted at q = 50 AU, rather than at its true perihelion distance of 78 AU.

TABLE 5. Geometric albedo.

		MPC Classification*		DES Classification†	
	All	Centaurs	KBOs	Centaurs	KBOs
Quantity		Statistics			
Average	8.01	6.55	8.87	6.30	9.88
Median	6.85	5.74	7.67	5.73	8.41
σ‡	4.07	2.68	4.22	2.50	4.23
# Obj.§	35	15	18	19	14

	Correlations									
Parameter	ρ¶	χ**	ρ¶	χ**	ρ¶	χ**	ρ¶	χ**	ρ¶	χ**
a	0.46	2.74	0.70	2.78	0.24	1.03	0.41	1.81	0.16	0.60
$q_\odot$	0.58	3.49	0.58	2.32	0.65	2.83	0.43	1.94	0.53	2.04
D	0.45	2.70	–0.08	0.32	0.77	3.37	–0.07	0.31	0.72	2.80
S	0.40	2.40	0.64	2.58	0.13	0.56	0.66	2.94	–0.08	0.32

*Centaurs classified as objects having orbital semimajor axes <30.066 AU.
†Centaurs classified by dynamical simulations [Deep Ecliptic Survey (*Elliot et al.,* 2005)].
‡Standard deviation of the albedo values.
§Number of Spitzer albedos used (from Table 4). The highest and lowest values were excluded.
¶Spearman rank correlation coefficient between albedo and the parameter in the left column.
**Significance of the correlation, in standard deviations relative to the null hypothesis.

The dichotomy between 136199 Eris, 136108 (2003 EL_{61}), 136472 (2005 FY_9), Pluto (and probably 90377 Sedna), and the rest of the KBOs and the Centaurs, in terms of their albedos and spectral characteristics, suggest that they are members of a unique physical class within the Kuiper belt population (see the chapter by Brown). We will refer to these objects as "planetoids" in the following, and generally exclude them from our discussion of albedo statistics and correlations because of their obviously unique character.

5.1. Albedo Statistics

Table 5 summarizes the statistics of the Spitzer-derived albedos, and the correlations between albedo and other parameters. Because there is no clearly preferred way to differentiate Centaurs from KBOs, we give results for two definitions: $a < 30.066$ AU (which we term the MPC Definition, referring to the Minor Planet Center classification) (see the chapter by Gladman et al.), and the DES Definition (referring to the Deep Ecliptic Survey classification) (*Elliot et al.,* 2005).

Typical geometric albedos for all of the KBOs and Centaurs are in the range 6.9–8.0%, depending on whether the mean or median is used, with a dispersion of about 4.1%. Regardless of which Centaur classification one chooses, it appears that Centaurs may have slightly lower albedos than KBOs, although the differences are not statistically significant relative to the dispersion of the albedos within the classes. The Kuiper variant of the Kolmogorov-Smirnov (K-S) test gives no evidence that the albedos of the KBOs and Centaurs are drawn from different parent populations, regardless of whether the MPC or DES definition of Centaur is used. Typical values for the beaming parameter (excluding results based on an assumed beaming parameter) are in the range 1.1–1.20, with a dispersion of about 0.4. This is in good agreement with the value of 1.2 ± 0.35 we adopted for the "KBO-tuned STM" used to construct Table 3. There does not appear to be any significant difference in the beaming parameter between KBOs and Centaurs.

5.2. Albedo Correlations

Because our errors are nonsymmetric and probably non-Gaussian, we apply the Spearman rank-correlation test to assess the significance of any correlations between albedo and other parameters. Table 5 gives the correlation coefficients (ρ) and their significance (χ) in standard deviations from the noncorrelated case. The albedos for the four planetoids mentioned above are not included in these calculations.

Figures 3a and 3b show p_V as a function of the orbital properties a and $q_\odot$. There is an upward trend of p_V vs. a, with the objects at $a < 20$ AU clustering at $p_V \simeq 5\%$, while at larger distances there is significantly more scatter in p_V. As shown in Table 5, the correlation between p_V and a for the entire sample is significant at the $\chi = 2.7\sigma$ level (99.4% likelihood). It appears that most of the correlation is due to the Centaurs, but the significance of the Centaur correlation depends considerably on which definition of Centaur is used. (Note that because the number of objects in the KBO and Centaur subsamples is about half that of the full sample, the significance of the correlations for the subsamples is typically lower than that for the full sample.) Because the significance of the p_V vs. a correlation is below 3σ, it is tentative. Another reason to treat the correlation with some skepticism is that it could reflect biases in the parameter

space for KBO discoveries: Low-albedo objects will be harder to detect at visible wavelengths, and the difficulty increases significantly with distance. Because our sample is drawn from optically discovered objects, one might expect a trend such as seen in Fig. 3a even if there is no real correlation between p_V and a.

Figure 3b reveals a similar correlation between p_V and $q_\odot$, and Table 5 suggests that in this case the correlation is significant at the $\chi = 3.5\sigma$ level (99.95% likelihood). This correlation holds up fairly well for both Centaurs and KBOs, regardless of which classification is used. It is possible that this correlation could also be due to the discovery bias mentioned above. However, if it reflects an actual relationship between p_V and q, there may be a fairly simple explanation. Objects closer to the Sun will tend to experience higher temperatures, depleting their surfaces of volatile molecules (which typically have high visible reflectances). Likewise, UV photolysis and solar wind radiolysis will also proceed more quickly closer to the Sun, and could darken those surfaces (although radiolysis by cosmic rays probably dominates beyond about 45 AU).

Figures 3c and 3d show p_V as a function of intrinsic properties of the objects: the diameter, D, and the visible spectral slope (color), S. Figure 3c shows an apparent correlation between p_V and D, and particularly so for the KBOs. This correlation is apparently confirmed in Table 5, where for the MPC classification the p_V vs. D correlation is significant at the $\chi = 3.4\sigma$ level (99.9% likelihood). However, for the DES classification the significance is only $\chi = 2.8\sigma$ (99.5% likelihood), so the correlation is not robust against small changes in which objects are considered as KBOs. Including the planetoids in the correlation calculation increases the significance of the correlation to well above 3σ, but doing so results in a (probably) false impression that the albedos of *all* KBOs are well correlated with diameter. At this time it is difficult to conclude that any such correlation exists at a statistically significant level.

Figure 3d shows an apparent correlation between p_V and S, particularly for the Centaurs. Table 5 shows that this correlation is the second most significant for a subclass, with $2.6 \le \chi \le 2.9$ (depending on the classification chosen), second only to the p_V vs. D correlation for KBOs. Here, the Kuiper variant K-S test does indicate a high likelihood (99.95%) that the albedos of red KBOs and Centaurs (with $S > 0.2$) are drawn from a different parent population than the gray ones, a similar result to that found based on the Centaur colors alone (see chapter by Tegler et al.). A natural assumption might be that the color diversity of KBOs and Centaurs results from mixing between icy (bright, spectrally neutral) and organic (dark, red) components. However, this correlation suggests that red objects systematically have higher albedos than the gray ones. On the basis of spectral mixing models between spectrally neutral dark materials (such as charcoal) and red material (represented by Titan tholin), *Grundy and Stansberry* (2003) suggested that just such a correlation between red color and higher albedo might exist. Why the Centaurs might embody this effect more strongly than the KBOs is still a mystery. Interestingly, the three most spectrally neutral objects defy the color-albedo trend, having rather high albedos: There may be at least two mechanisms underlying the observed color diversity. Those objects are 2060 Chiron, 90482 Orcus, and (2003 AZ_{84}), and their unique position in the albedo-color plane may indicate that they share some unique surface character.

6. FUTURE PROSPECTS

At present, Spitzer/MIPS provides the most sensitive method available for measuring thermal fluxes from typical KBOs, but several upcoming observatories and instruments will provide substantially improved sensitivity. The joint ESA/NASA Herschel mission will have at least a factor of 2 better sensitivity at 75 μm (compared to the 70-μm sensitivity of MIPS), and will additionally have a number of photometry channels in the range 70–500 μm. Since cold KBOs have their thermal emission peaks in the range 60–100 μm, observations in the Herschel band passes will map the peak of a KBO SED. Herschel is scheduled for launch in late 2008. The Large Millimeter Telescope (LMT) in central Mexico will have sufficient sensitivity at 1 mm with the SPEED instrument to detect thermal flux from the Rayleigh-Jeans tail of cold KBOs. First light for the LMT is expected in 2008.

Farther in the future, the American-European-Chilean Atacama Large Millimeter Array (ALMA) will provide sufficient sensitivity from 0.35 to 3 mm to detect typical KBOs; first light for ALMA might be as soon as 2012. The Cornell Caltech Atacama Telescope (CCAT) will operate at 200 μm to 1 mm, and its sensitivity at 350 μm will surpass that of ALMA; first light could also be in 2012. Any of Herschel, ALMA, and CCAT (the case is less convincing for the LMT) could be used for a large survey of many moderate-sized (100-km-class) KBOs. Such a program would expand the number of KBOs with good thermal measurements (and therefore radii and albedos) from tens to hundreds.

All these next-generation capabilities operate at wavelengths either near the emission peak of KBOs, or well out on the Rayleigh-Jeans part of their spectra. While albedos and diameters derived from such observations are less model-dependent than those based on single-wavelength observations taken shortward of the emission peak, there are still significant uncertainties. For example, canonical STM and ILM fits to an 850-μm flux density produce albedos that differ by about 30%; if the KBO-tuned STM is used (including its uncertainty on η), that uncertainty is cut almost in half. If the validity of the KBO-tuned STM is born out by further Spitzer observations of KBOs, it can be used to significantly refine the albedos and diameters derived from submillimeter KBO detections.

7. SUMMARY

Efforts to characterize the physical properties of KBOs and Centaurs with Spitzer are beginning to pay off. Considerable improvements have been made in the first three

years of the mission in terms of predicting the necessary integration times, developing aggressive and successful observing strategies, and data processing. We present our 24- and 70-μm observations for 47 targets (31 with orbital semimajor axes larger than that of Neptune, 16 inside Neptune's orbit), and apply a modified version of the standard thermal model to derive albedos and diameters for them. Thirty-nine of the targets were detected at signal-to-noise ratios ≥5 at one or both wavelengths. We use that sample to look for relationships between albedo and the orbital and physical parameters of the objects. The most marked such relationship is the distinct discontinuity in albedo at a diameter of about 1000 km, with objects larger than that having albedos in excess of 60%, and those smaller than that having albedos below about 25%. We suggest that these large, very-high-albedo objects [90377 Sedna, 136108 (2003 EL_{61}), 136199 Eris, and 136472 (2005 FY_9)] constitute a distinct class in terms of their physical properties.

The data suggest possible correlations of albedo with orbital distance, and with size and color, but the statistical significance of the correlations is marginal. Two correlations, those of albedo with perihelion distance (for KBOs and Centaurs) and with diameter (for KBOs), are nominally significant at more than the 3σ level. Perhaps the most interesting trend (albeit significant at only about the 2.8σ level) is for distinctly red Centaurs to have higher albedos than those that are more gray, contrary to what might intuitively be expected.

Prospects for improving on and expanding these results are relatively good. Spitzer will be operational into 2009, and more KBO observations will probably be approved. New ground- and spacebased observatories will also contribute significantly, and at wavelengths that are complementary to those used here. In particular, submillimeter to millimeter studies of KBOs should be relatively easy with facilities such as ALMA, CCAT, and LMT. The Herschel mission should also be very productive at far-IR to submillimeter wavelengths.

Acknowledgments. Many of the results presented here are based on observations made with the Spitzer Space Telescope, which is operated by the Jet Propulsion Laboratory, California Institute of Technology, under contract with NASA. Support for this work was provided through multiple awards issued by JPL. Online resources offered by the Solar System Dynamics group at JPL and the Minor Planet Center of the International Astronomical Union were extremely valuable.

REFERENCES

Altenhoff W. J., Menten K. M. and Bertoldi F. (2002) Size determination of the Centaur Chariklo from millimeter-wavelength bolometer observations. *Astron. Astrophys., 366,* L9–12.

Altenhoff W. J., Bertoldi F., and Menten K. M. (2004) Size estimates of some optically bright KBOs. *Astron. Astrophys., 415,* 771–775.

Barucci M. A., Boehnhardt H., Dotto E., Doressoundiram A., Romon J., et al. (2002) Visible and near-infrared spectroscopy of the Centaur 32532 (2001 PT_{13}). ESO Large Program on TNOs and Centaurs: First spectroscopy results. *Astron. Astrophys., 392,* 335–339.

Barucci M. A., Cruikshank D.P., Dotto E., Merlin F., Poulet F., et al. (2005) Is Sedna another Triton? *Astron. Astrophys., 439,* L1–L4.

Bauer J. M., Meech K. J., Fernandez Y. R., Pittichova J., Hainaut O. R., Boehnhardt H., and Delsanti A. (2003) Physical survey of 24 Centaurs with visible photometry. *Icarus, 166,* 195–211.

Bertoldi F., Altenhoff W., Weiss A., Menten K. M., and Thum C. (2006) The trans-Neptunian object UB_{313} is larger than Pluto. *Nature, 439,* 563–564.

Bowell E., Hapke B., Domingue D., Lumme K., Peltoniemi J., and Harris A. (1989) Application of photometric models to asteroids. In *Asteroids II* (R. P. Binzel et al., eds.), pp. 524–556. Univ. of Arizona, Tucson.

Brown M. E. and Trujillo C. A. (2004) Direct measurement of the size of the large Kuiper belt object (50000) Quaoar. *Astron. J., 127,* 2413–2417.

Brown M. E., Trujillo C. A., Rabinowitz D., Stansberry J., Bertoldi F., and Koresko C. D. (2004) A Sedna update: Source, size, spectrum, surface, spin, satellite. *Bull. Am. Astron. Soc., 36,* 1068.

Brown M. E., Trujillo C. A., and Rabinowitz D. L. (2005) Discovery of a planetary-sized object in the scattered Kuiper belt. *Astrophys. J. Lett., 635,* L97–L100.

Brown M. E., Schaller E. L., Roe H. G., Rabinowitz D. L., and Trujillo C. A. (2006) Direct measurement of the size of 2003 UB_{313} from the Hubble Space Telescope. *Astrophys. J. Lett., 643,* L61–L63.

Brown M. E., Barkume K. M., Blake G. A., Schaller E. L., Rabinowitz D. L., Roe H. G., and Trujillo C. A. (2007) Methane and ethane on the bright Kuiper belt object 2005 FY_9. *Astron. J., 133,* 284–289.

Brown R. H., Cruikshank D. P., and Pendleton Y. (1999) Water ice on Kuiper belt object 1996 TO_{66}. *Astrophys. J. Lett., 519,* L101–L104.

Campins H., Telesco C. M., Osip D. J., Rieke G. H., Rieke M. J., and Shulz B. (1994) The color temperature of (2060) Chiron: A warm and small nucleus. *Astron. J., 108,* 2318–2322.

Cruikshank D. P. and Brown R. H. (1983) The nucleus of comet P/Schwassmann-Wachmann 1. *Icarus, 56,* 377–380.

Cruikshank D. P., Stansberry J. A., Emery J. P., Fernández Y. R., Werner M. W., Trilling D. E., and Rieke G. H. (2005) The high-albedo Kuiper belt object (55565) 2002 AW_{197}. *Astrophys J., 624,* L53–L56.

Cruikshank D. P., Barucci M. A., Emery J. P., Fernández Y. R., Grundy W. M., Noll K. S., and Stansberry J. A. (2006) Physical properties of transneptunian objects. In *Protostars and Planets V* (B. Reipurth et al., eds.), pp. 879–893. Univ. of Arizona, Tucson.

Davies J., Spencer J., Sykes M., Tholen D., and Green S. (1993) (5145) Pholus. *IAU Circular 5698.*

de Bergh C., Boehnhardt H., Barucci M. A., Lazzarin M., Fornasier S., et al. (2004) Aqueous altered silicates at the surface of two Plutinos? *Astron. Astrophys., 416,* 791–798.

Delbo M., Harris A. W., Binzel R. P., Pravec P., and Davies J. K. (2003) Keck observations of near-Earth asteroids in the thermal infrared. *Icarus, 166,* 116–130.

Elliot J. L., Kern S. D., Clancy K. B., Gulbis A. A. S., Millis R. L., et al. (2005) The Deep Ecliptic Survey: A search for Kuiper belt objects and Centaurs. II. Dynamical classification, the Kuiper belt plane, and the core population. *Astron. J., 129,* 1117–1162.

Emery J. P., Dalle Ore C. M., Cruikshank D. P., Fernández Y. R., Trilling D. E., and Stansberry J. A. (2007) Ices on (90377) Sedna: Confirmation and compositional constraints. *Astron. Astrophys., 466,* 395–398.

Engelbracht C. W., Blaylock M., Su K. Y. L., Rho J., Rieke G. H., et al. (2007) Absolute calibration and characterization of the Multiband Imaging Photometer for Spitzer. I. The stellar calibrator sample and the 24 micron calibration. *Publ. Astron. Soc. Pac.,* in press.

Fernández Y. R., Jewitt D. C., and Sheppard S. S. (2002) Thermal properties of Centaurs Asbolus and Chiron. *Astron. J., 123,* 1050–1055.

Fernández Y. R., Sheppard S. S., and Jewitt D. C. (2003) The albedo distribution of jovian Trojan asteroids. *Astron. J., 126,* 1563–1574.

Fornasier S., Doressoundiram A., Tozzi G. P., Barucci M. A., Boehnhardt H., et al. (2004) ESO Large Program on Physical Studies of Trans-Neptunian Objects and Centaurs: Final results of the visible spectrophotometric observations. *Astron. Astrophys., 421,* 353–363.

Gordon K. G., Engelbracht C. W., Fadda D., Stansberry J. A., Wacther S., et al. (2007) Absolute calibration and characterization of the Multiband Imaging Photometer for Spitzer II. 70 micron imaging. *Publ. Astron. Soc. Pac.,* in press.

Groussin O., Lamy P., and Jorda L. (2004) Properties of the nuclei of Centaurs Chiron and Chariklo. *Astron. Astrophys., 413,* 1163–1175.

Grundy W. M. and Stansberry J. A. (2003) Mixing models, colors, and thermal emissions. *Earth Moon Planets, 92,* 331–336.

Grundy W. M., Noll K. S., and Stephens D. C. (2005) Diverse albedos of small trans-neptunian objects. *Icarus, 176,* 184–191.

Grundy W. M., Stansberry J. A., Noll K. S., Stephens D. C., Trilling D. E., Kern S. D., Spencer J. R., Cruikshank D. P., and Levison H. F. (2007) The orbit, mass, size, albedo, and density of (65489) Ceto-Phorcys: A tidally-evolved binary Centaur. *Icarus,* in press.

Harris A. W. (1998) A thermal model for near-Earth asteroids. *Icarus, 131,* 291–301.

Horner J., Evans N. W., and Bailey M. E. (2004) Simulations of the population of Centaurs — I. The bulk statistics. *Mon. Not. R. Astron. Soc., 354,* 798–810.

Jewitt D. C. and Luu J. X. (1993) Discovery of the candidate Kuiper belt object 1992 QB_1. *Nature, 362,* 730–732.

Jewitt D. C., Aussel H., and Evans A. (2001) The size and albedo of the Kuiper-belt object (20000) Varuna. *Nature, 411,* 446–447.

Jones T. J. and Morrison D. (1974) Recalibration of the photometric/radiometric method of determining asteroid sizes. *Astron. J., 79,* 892–895.

Lazzarin M., Barucci M. A., Boehnhardt H., Tozzi G. P., de Bergh C., and Dotto E. (2003) ESO Large Programme on Physical Studies of Trans-Neptunian Objects and Centaurs: Visible spectroscopy. *Astrophys. J., 125,* 1554–1558.

Lebofsky L. A. and Spencer J. R. (1989) Radiometry and thermal modeling of asteroids. In *Asteroids II* (R. P. Binzel et al., eds.), pp. 128–147. Univ. of Arizona, Tucson.

Lebofsky L. A., Sykes M. V., Tedesco E. F., Veeder G. J., Matson D. L., et al. (1986) A refined 'standard' thermal model for asteroids based on observations of 1 Ceres and 2 Pallas. *Icarus, 68,* 239–251.

Lellouch E., Laureijs R., Schmitt B., Quirico E., de Bergh C., et al. (2000) Pluto's non-isothermal surface. *Icarus, 147,* 220–250.

Lellouch E., Moreno R., Ortiz J. L., Paubert G., Doressoundiram A., and Peixinho N. (2002) Coordinated thermal and optical observations of trans-neptunian object (20000) Varuna from Sierra Nevada. *Astron. Astrophys., 391,* 1133–1139.

Levison H. F. and Duncan M. J (1997) From the Kuiper belt to Jupiter-family comets: The spatial distribution of ecliptic comets. *Icarus, 127,* 13–32.

Licandro J., Pinilla-Alonso N., Pedani M., Oliva E., Tozzi G. P., and Grundy W. M. (2006a) The methane ice rich surface of large TNO 2005 FY_9: A Pluto-twin in the trans-neptunian belt? *Astron. Astrophys., 445,* L35–L38.

Licandro J., Grundy W. M., Pinilla-Alonso N., and Leysi P. (2006b) Visible spectroscopy of TNO 2003 UB_{313}: Evidence for N_2 ice on the surface of the largest TNO? *Astron. Astrophys., 458,* L5–L8.

Margot J. L., Brown M. E., Trujillo C. A., and Sari R. (2002) The size and albedo of KBO 2002 AW_{197} (abstract). *Bull. Am. Astron. Soc., 34,* 871.

Margot J. L., Brown M. E., Trujillo C. A., and Sari R. (2004) HST observations of Kuiper belt binaries (abstract). *Bull. Am. Astron. Soc., 36,* 1081.

Merlin F., Barucci M. A., Dotto E., de Bergh C., and Lo Curto G. (2005) Search for surface variations on TNO 47171 and Centaur 32532. *Astron. Astrophys., 444,* 977–982.

Morrison D. and Lebofsky L. A. (1979) Radiometry of asteroids. In *Asteroids* (T. Gehrels, ed.), pp. 184–205. Univ. of Arizona, Tucson.

Morrison D., Owen T., and Soderblom L. A. (1986) The satellites of Saturn. In *Satellites* (J. A. Burns and M. S. Matthews, eds.), pp. 764–801. Univ. of Arizona, Tucson.

Noll K. S., Stephens D. C., Grundy W. M., and Griffin I. (2004) The orbit, mass, and albedo of trans-neptunian binary (66652) 1999 RZ_{253}. *Icarus, 172,* 402–407.

Ortiz J. L., Sota A., Moreno R., Lellouch E., Biver N., et al. (2004) A study of trans-neptunian object 55636 (2002 TX_{300}). *Astron. Astrophys., 420,* 383–388.

Osip D. J., Kern S. D., and Elliot J. L. (2003) Physical characterization of the binary Edgeworth-Kuiper belt object 2001 QT_{297}. *Earth Moon Planets, 92,* 409–421.

Rabinowitz D. L., Barkume K., Brown M. E., Roe H., Schwartz M., et al. (2005) Photometric observations constraining the size, shape, and albedo of 2003 EL_{61}, a rapidly rotating, Pluto-sized object in the Kuiper belt. *Astrophys. J., 639,* 1238–1251.

Rieke G. H., Young E. T., Engelbracht C. W., Kelly D. M., Low F. J., et al. (2004) The Multiband Imaging Photometer for Spitzer (MIPS). *Astrophys. J. Suppl., 154,* 25–29.

Romanishin W. and Tegler S. C. (2005) Accurate absolute magnitudes for Kuiper belt objects and Centaurs. *Icarus, 179,* 523–526.

Schaller E. L. and Brown M. E. (2007) Volatile loss and retention on Kuiper belt objects and the depletion of nitrogen on 2005 FY_9. *Astrophys. J. Lett., 659,* L61–L64.

Spencer J. R. (1990) A rough-surface thermophysical model for airless planets. *Icarus, 83,* 27–38.

Stansberry J. A., Van Cleve J., Reach W. T., Cruikshank D. P., Emery J. P., et al. (2004) Spitzer observations of the dust coma and nucleus of 29P/Schwassmann-Wachmann 1. *Astrophys. J. Suppl., 154,* 463–468.

Stansberry J. A., Grundy W. M., Margot J. L., Cruikshank D. P., Emery J. P., et al. (2006) The albedo, size, and density of binary Kuiper belt object (47171) 1999 TC_{36}. *Astrophys. J., 643,* 556–566.

Stansberry J. A., Gordon K. D., Bhattacharya B., Engelbracht

C. W., Rieke G. H., et al. (2007) Absolute calibration and characterization of the Multiband Imaging Photometer for Spitzer III. An asteroid-based calibration at 160 microns. *Publ. Astron. Soc. Pac.,* in press.

Sykes M. V. (1999) IRAS survey-mode observations of Pluto-Charon. *Icarus, 142,* 155–159.

Sykes M. V. and Walker R. G. (1991) Constraints on the diameter and albedo of Chiron. *Science, 251,* 777–780.

Tedesco E. F., Veeder G. J., Fowler J. W., and Chillemi J. R. (1992) *The IRAS Minor Planet Survey.* Phillips Lab. Tech. Report PL-TR-92-2049, Hanscom AFB, Massachussettes.

Tedesco E. F., Noah P. V., Noah M., and Price S. D. (2002) The supplemental IRAS Minor Planet Survey. *Astron. J., 123,* 1056–1085.

Tegler S. C., Grundy W. M., Romanishin W., Consolmagno G. J., Mogren K., and Vilas F. (2007) Optical spectroscopy of the large Kuiper belt objects 136472 (2005 FY_9) and 136108 (2003 EL_{61}). *Astron. J., 133,* 526–530.

Thomas N., Eggers S., Ip W.-H., Lichtenberg G., Fitzsimmons A., Jorda L., et al. (2000) Observations of the trans-neptunian objects 1993 SC and 1996 TL_{66} with the Infrared Space Observatory. *Astrophys. J., 534,* 446–455.

Trilling D. E. and Bernstein G. M. (2006) Light curves of 20–100 km Kuiper belt objects using the Hubble Space Telescope. *Astron. J., 131,* 1149–1162.

Veillet C., Parker J. W., Griffin I., Marsden B., Doressoundiram A., et al. (2002) The binary Kuiper-belt object 1998 WW_{31}. *Nature, 416,* 711–713.

Werner M. W., Roellig T. L., Low F. J., Rieke G. H., Rieke M. J., et al. (2004) The Spitzer Space Telescope mission. *Astrophys. J. Suppl., 154,* 1–9.